First Principles Modeling of the Thermodynamic and Kinetic Properties of Anatase Li_xTiO_2 and the Ti-Al Alloy System With Dilute Vacancies

by

Anna A. Belak

A dissertation submitted in partial fulfillment
of the requirements for the degree of
Doctor of Philosophy
(Materials Science and Engineering)
in The University of Michigan
2014

Doctoral Committee:

Associate Professor Anton Van der Ven, Co-Chair, University of California Santa Barbara
Assistant Professor Emmanouil Kioupakis, Co-Chair
Professor John Edmond Allison
Assistant Professor Bart Bartlett

For Maxine Turner, whose memory compels us to press on.

ACKNOWLEDGEMENTS

While my journey through higher education has mostly been an exciting and fortunate one, there is a number of people without whom it would undoubtedly have been less successful. Primarily, of course, I must express my utmost gratitude to my adviser, Prof. Anton Van der Ven, whose careful guidance, unrivaled teaching skills, and infinite patience created a most pleasant and fulfilling graduate school experience. Anton's consistent stream of gentle motivational prodding through multitudes of setbacks and sincere enthusiasm for all of my mini-discoveries made him a fantastic mentor.

My committee members, Professors Emmanouil Kioupakis, John Allison, and Bart Barlett have, to varying degrees, served to provide fresh perspectives on my work and challenge me to consider how the problems I am working on may be approached from different disciplines. Their collective mentorship and support have been invaluable, and I thank them especially for the many lively and humorous discussions over the years, about both work and life in general.

I must acknowledge the generous funding from the Rackham Graduate School through the Rackham Merit Fellowship, and extend a special thanks to all of the staff at Rackham and in the Materials Science Department for their help throughout the years. Most notably, I have to say that without Renee Hilgendorf's tireless assistance, navigating the administrative requirements would have been a total nightmare.

I would like to thank all of the faculty who have taught and mentored me, academically and otherwise, at the University of Michigan. I must express particular gratitude to Professors Max Shtein, Rachel Goldman, and John Kieffer, who have also become my good friends and been remarkably encouraging during the tougher parts of my tenure here.

I have immensely enjoyed the company of my colleagues and have at times learned much more from interactions with them than from any coursework. I especially appreciated the collaborative and friendly environment in the AVDV lab, and owe a huge thank you in particular to John Thomas for alleviating much of my frustration with often very simple and elegant solutions to my overcomplicated problems.

Certainly, I am also grateful to my friends and family for listening to me complain, making me laugh, boosting my confidence, and generally keeping my spirits high.

Lastly, but most importantly, I want to thank my mother, Maija Kukla, for teaching me almost everything I know, inspiring me to pursue a Ph.D. at some point in kindergarden, and supporting this crazy ambition for the following two decades. I definitely could not have accomplished half of the things that I did without her skillful parenting and warm friendship.

TABLE OF CONTENTS

LIST OF FIGURES

Figure

LIST OF TABLES

Table

LIST OF ABBREVIATIONS

DFT Density Functional Theory

HF Hartree-Fock

LDA Local Density Approximation

GGA Generalized Gradient Approximation

PBE Perdew, Burke, and Ernzerhof

LAPW Linear Augmented Plane Wave

PAW Projector Augmented Wave

VASP Vienna Ab-initio Simulation Package

CLEX Cluster Expansion

ECI Effective Cluster Interactions

RMS Root Mean Square

CV Cross-Validation

CASM Cluster Assisted Statistical Mechanics

NEB Nudged Elastic Band

KRA Kinetically Resolved Activation Barrier

KMC Kinetic Monte Carlo

HCP Hexagonal Close Packed

FCC Face Centered Cubic

BCC Body Centered Cubic

ABSTRACT

First Principles Modeling of the Thermodynamic and Kinetic Properties of Anatase Li_xTiO_2 and the Ti-Al Alloy System With Dilute Vacancies

by

Anna A. Belak

Co-Chairs: Anton Van der Ven and Emmanouil Kioupakis

We perform a comprehensive first-principles statistical mechanical study of the thermodynamic and kinetic properties of two separate materials systems with very different applications using a collection of reliable computational methods.

Anatase TiO_2 can be lithiated to Li_xTiO_2 and has thus been a candidate material for Li-ion battery electrodes for quite some time. We establish that the experimentally observed step in the voltage vs lithium composition curve between $x = 0.5$ and 0.6 is due to Li ordering. Furthermore, we predict that full lithiation of anatase TiO_2 is thermodynamically possible at positive voltages but that there is an enormous difference in Li diffusion coefficients in the dilute and fully lithiated forms of TiO_2, providing an explanation for the limited capacity in large electrode particles. We also predict that Li diffusion in the ordered phase ($Li_{0.5}TiO_2$) is strictly one-dimensional. The TiO_2 to $Li_{0.5}TiO_2$ phase transition has much in common with shape memory alloys. Crystallographically, it can support strain invariant interfaces separating TiO_2 and $Li_{0.5}TiO_2$ within the same particle. The strain invariant interfaces are parallel to the one-dimensional diffusion direction in $Li_{0.5}TiO_2$, which, we argue, has important consequences for the role of particle shape on achievable capacity, charge and discharge rates, and hysteresis.

The titanium-aluminum alloy system has many important structural applications in the automotive and aerospace realms. Variations in alloy concentration or the degree of short or long range order affect the vacancy concentration and thereby the mobility of the constituents of the alloy. Here we develop statistical mechanical methods to predict the thermodynamic properties of vacancies within multi-component

solids from first principles. We introduce a coarse graining procedure that enables the prediction of very dilute vacancy concentrations and their associated thermodynamic properties with Monte Carlo simulations. We apply this approach to a study of vacancies in HCP based Ti-Al binary alloys to explore the role of variations in both short range and long range order on the equilibrium vacancy concentration. We find a strong dependence of the equilibrium vacancy concentration on Al concentration and degree of long range order, especially at low temperature.

CHAPTER I

Introduction

Computational methods have come a long way since their conception in the early 20th century. The first *ab initio* approach was invented by Douglas Hartree in the 1920s[1], and the first Monte Carlo algorithm was designed in the 1940s by Metropolis and Ulam[2]. Just four years later, Werner Heisenberg was awarded the Nobel Prize in Physics for the creation of quantum mechanics. As the depth of our understanding of quantum and solid state physics grew and ever cheaper and faster computational machines began to emerge, increasingly powerful theoretical models developed alongside them. By the 1950s, computers were finally good enough to apply Hartree's original idea to calculations of small molecules. From here, Hartree-Fock theory evolved, to be later joined by Density Functional Theory (DFT) in the 1970s, but it was not until the 1990s that these methods became widely accepted as sufficiently accurate for quantum chemical calculations. Today, computational methods are many and varied, and they are considered an essential component of any serious scientific endeavor. Our ability not only to confirm and explain experimental findings, but also to predict and elucidate phenomena not accessible to measurement techniques, make computational modeling an invaluable tool for science and engineering in the 21st century. The methodology used in this work is presented primarily in Chapter II.

1.1 Insertion Compounds for Li-ion Battery Electrodes

Rechargeable lithium-ion batteries have become extremely popular since they were first commercially introduced in the early 1990s. They are used today in a vast array of electronic devices ranging from cell phones and laptops to electric cars and backup power generators. Though rechargeable lithium-ion battery technology is widespread, fairly well developed, and easily accessible, there is plenty of room for improvement in the design of the various cell components. A typical Li-ion battery consists of three

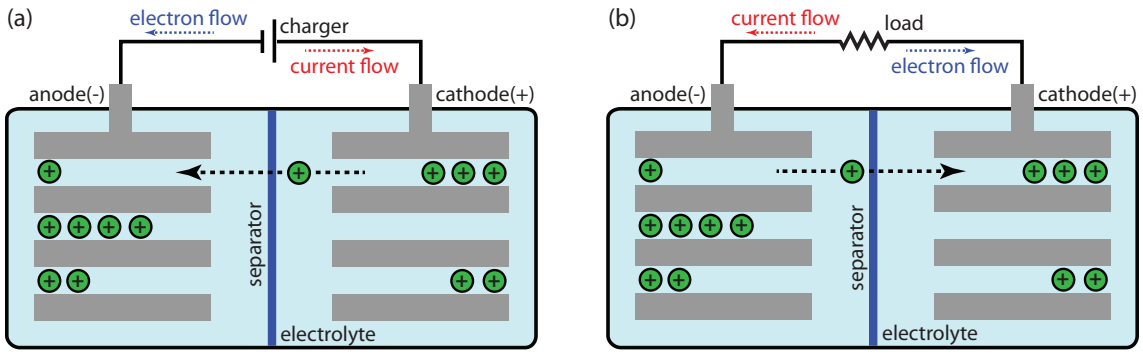

Figure 1.1. Schematic drawing depicting the Li-ion operating mechanism. The charging process is shown in (a), and discharging is shown in (b).

major parts: the anode, the cathode, and the electrolyte. As shown in Figure 1.1, this device works by shuttling ions from one electrode to the other. The voltage of the battery is determined by difference in the chemical potential of lithium in the anode and the cathode. To charge the battery, a current is applied, forcing the negatively charged electrons to flow to the anode, which in turn pulls the positively charged lithium ions through the electrolyte in the same direction (Figure 1.1a). One of the required characteristics of the electrolyte material is that it must be ionically conducting but electronically insulting, such that only the lithium is allowed to move through it (unlike the electrodes, which mush readily conduct both electrons and lithium ions). When the battery is discharged, a similar process occurs in the opposite direction. A load is applied to the circuit, lithium ions move toward the cathode through the electrolyte, and a current is generated in the opposite direction (Figure 1.1b). The electrolyte is perhaps the messiest of the battery components. Most electrolytes used today are non-aqueous solvents (which tend to be flammable) containing a lithium salt. This makes them moderately difficult to handle and package as well as potentially dangerous if damaged. In the realm of electrodes, graphite is by far the most popular anode material, though recently silicon has also made an appearance. Cathodes are usually made from either a layered metal oxide (e.g. lithium cobalt oxide), a polyanion (e.g. lithium iron phosphate), or a spinel (e.g. lithium manganese oxide). The focus of the work described in Chapter III is on lithium titanium dioxide (anatase TiO_2) as a potential anode material (due to its relatively low voltage) for rechargeable lithium ion batteries. These materials are chosen for their open crystal structures that allow them to accommodate a large number of guest lithium ions, resulting in a high capacity for the battery.

Though the charge-discharge process may seem quite simple on the macro scale, a number of important thermodynamic and kinetic phenomena can affect its effec-

tiveness. Beyond just high theoretical capacity, for example, it is important that the ions are able to quickly and efficiently diffuse into and out of the electrodes. As the lithium composition within an electrode increases, the host material may undergo a phase transformation to a more energetically favorable structure, which could have negative effects on the usefulness of the device. Additionally, lithium concentration changes can affect the electronic properties of the host material, which can lead to structural distortions (e.g. Jahn-Teller), decreased conductivity, or other issues.

Another crucial aspect is the actual diffusivity of the lithium atoms within the electrode host. The Li mobility determines the rate at which ions can be inserted into and removed from the electrodes (and therefore how quickly the battery can charge and discharge). Both the actual magnitude of the diffusion coefficient and the likely directions of mobility can be a function of the lithium composition and the degree of lithium-vacancy disorder and short range order. We use a combination of first principles and statistical mechanical methods to provide a detailed description of these phenomena. This work has been published previously in the journal *Chemistry of Materials* [3].

1.2 Titanium-Aluminum Structural Alloys

The titanium-aluminum alloy system has been of interest primarily in the realm of automotive and aerospace applications for quite some time. Structural alloys in general and Ti-Al in particular continue to gain popularity due to many favorable materials properties such as high melting temperature, high yield strength at high temperatures, good resistance to oxidation and corrosion, and advanced creep characteristics [4, 5]. Ti-Al alloys could potentially replace the traditional Ni based superalloys in aircraft engines, which are nearly twice as dense, greatly improving the thrust-to-weight ratio.

The history of the Ti-Al binary phase diagram is riddled with controversy. The first, and perhaps most frequently cited, incarnation of it was published in 1987 by Murray [6], and although many of the proposed phase boundaries in this version were purely speculative (and appeared as drawn-in dashed lines), subsequent reports often assumed them to be real. The relationships between α-Ti, β-Ti, α_2-Ti_3Al, and γ-TiAl phases in particular have sparked a great deal of intense debate over the years, which has not been fully put to rest due to the many difficulties, both experimentally and computationally, of describing those interactions[7].

Ti-rich titanium-aluminum serves as a very good model system for the develop-

ment of computational methods for modeling defects and diffusion in multi-component solids. It yields particularly nicely to the cluster expansion formalism due to the consistent HCP-type structure of the ground states between $x_{Al} = 0$ and $x_{Al} = 0.3$, which then allows us to employ some powerful statistical mechanical methods to consider the equilibrium vacancy composition in this alloy at a wide range of temperatures. The coarse grained Monte Carlo approach designed specifically for this study at low temperatures is discussed in detail in Chapter IV.

CHAPTER II

Theoretical Background and Computational Methods

2.1 Thermodynamics and Statistical Mechanics Basics

The thermodynamic properties of solids are macroscopic quantities that can describe very complex systems without being explicitly aware of the underlying microscopic interatomic interactions governing the relevant physical phenomena. In reality, because equilibrium quantities are time-independent, they are actually averages over the microstates of the system. A microstate σ is a particular state or excitation (e.g. configurational, vibrational) that the system can sample, and each state has a specific energy E_σ associated with it. We obtain this energy by solving the Schrödinger equation for a specific microstate.

The probability that a solid is in some microstate σ at constant temperature (T), volume (V), and number of atoms (N) is given by

$$P(\sigma) = \frac{1}{Z} e^{-E_\sigma / k_B T}, \tag{2.1}$$

where k_B is the Boltzmann constant and Z is the canonical partition function [8]

$$Z = \sum_\sigma e^{-E_\sigma / k_B T}. \tag{2.2}$$

In a sense, Equation 2.1 is a distribution function that determines which states are the most important in determining the thermodynamic averages we are after. It can also be thought of as indicating the amount of time that the system spends in a

particular state. Thus, average thermodynamic quantities can be calculated via

$$A = \sum_{\sigma} A_{\sigma} P_{\sigma}. \tag{2.3}$$

Here, A is some macroscopic quantity, and A_{σ} is its value when the system occupies microstate state σ. Additionally, the Gibbs free energy of a system is given by [9]

$$G = -k_B T \ln(Z). \tag{2.4}$$

This is essential for the prediction of phase stability, which is determined by examining the relative free energies of different phases at various temperatures. Thermodynamic equilibrium is represented by the minimum of the Gibbs free energy. To fully and accurately evaluate Equations 2.1–2.4, we need to access E_{σ} for all possible states σ of the system, which can include any number of configurational, vibrational, and electronic excitations. It would be nice to calculate all of these energies from first principles, but because the number of possible excitations is incredibly large, we instead resort to a model that allows us to extrapolate the first principles data for a limited number of possible excitations to describe any imaginable microstate.

2.2 First-principles Calculations

To determine the energy E_{σ} that corresponds to a particular microstate, we must solve the many-body Schröndinger equation for the crystal

$$\hat{H}\psi = E\psi, \tag{2.5}$$

which is an eigenvalue problem where $\hat{H}$ is the Hamiltonian operator for the system, ψ is a many-body wave function for the configuration, and E is the total energy of the crystal. Although it is possible to solve this equation and obtain the allowed eigenstates and energies by diagonalization, such an approach would be extremely computationally demanding. It is therefore usual to instead introduce an approximation based on a number of simplifying assumptions. The Born-Oppenheimer approximation allows us to assume that the ion and electron wave functions are independent due to the large difference in their masses, and thus the ion positions are assumed to be fixed with respect to the electron wave function [10].

While it is well known that the many-body problem is not solvable for realistic solids, there exist multiple approximation approaches that yield rather decent re-

sults. Among them is the Hartree-Fock (HF) approach, DFT, and various hybrid methods[11]. Of these, HF ignores the correlation effect caused by the electrostatic repulsion between electrons (e.g. it does not disallow two electrons from occupying the same position in space) and tends to be more computationally expensive than DFT. Meanwhile, DFT encounters the difficulty of not having access to the exact exchange and correlation functionals (for anything that is not a free electron gas), requiring further approximations. Hybrid functionals address this problem by allowing for the inclusion of the exchange energy as it is calculated in Hartree-Fock theory, but these methods are, consequently, the most computationally demanding. For all of the first principles calculations in this work, we elect to use the Density Functional Theory approach due to its versatility, low computational cost, and satisfactory results.

2.2.1 Density Functional Theory

We know from basic quantum mechanics that all of the information about a system is hidden inside its wave function Ψ, and that if we calculate this wave function from the Schrödinger equation, we can gain access to observables by taking expectation values of operators with this function, i.e.

$$V(\mathbf{r}) \xrightarrow{SE} \Psi(\mathbf{r}_1, \mathbf{r}_2, ..., \mathbf{r}_N) \xrightarrow{\langle\Psi|...|\Psi\rangle} \text{observables}, \tag{2.6}$$

where $V(r)$ is the potential chosen to specify the system. One of the observables we can calculate this way is the electron density

$$\rho(\mathbf{r}) = N \int d^3\mathbf{r}_2 \int d^3\mathbf{r}_3 ... \int d^3\mathbf{r}_N \Psi^*(\mathbf{r}, \mathbf{r}_2, ..., \mathbf{r}_N)\Psi(\mathbf{r}, \mathbf{r}_2, ..., \mathbf{r}_N), \tag{2.7}$$

and in DFT, this becomes the key variable.

$$\rho(\mathbf{r}) \longrightarrow \Psi(\mathbf{r}_1, \mathbf{r}_2, ..., \mathbf{r}_N) \longrightarrow V(\mathbf{r}) \tag{2.8}$$

As knowledge of $\rho(\mathbf{r})$ implies knowledge of the wave function, it also implies knowledge of all other observables. The core elements of DFT are the Hohenberg-Kohn theorems [12] and the Kohn-Sham equations [13]. The Hohenberg-Kohn theorem states that given a ground state density $\rho_0(\mathbf{r})$, it is possible to calculate the corresponding wave function $\Psi_0(\mathbf{r}_1, \mathbf{r}_2, ..., \mathbf{r}_N)$. (However, this theorem only proves existence and does not

provide an algorithm). This means that Ψ is a functional of ρ, denoted

$$\Psi = \Psi[\rho](\mathbf{r}_1, \mathbf{r}_2, ..., \mathbf{r}_N), \tag{2.9}$$

which indicates that Ψ is a function of its N spatial variables, but a *functional* of $\rho(\mathbf{r})$[11]. The electron density

$$\rho(\mathbf{r}) = \langle \Psi | \sum_j \delta(\mathbf{r} - \mathbf{r}_j) | \Psi \rangle \tag{2.10}$$

uniquely determines the ground state properties of the crystal. Likewise, all other ground state wave functions and expectation values are also functionals of the particle density. Then the ground state energy can be written as

$$E[\rho] = T[\rho] + U[\rho] + \int V(\mathbf{r})\rho(\mathbf{r}) d^3\mathbf{r}. \tag{2.11}$$

Here, $T[\rho]$ and $U[\rho]$ are universal operators (same for any system) for the kinetic energy and the electron-electron interaction. The external potential $V[\rho]$ is fully system-dependent (non-universal). If $T[\rho]$ and $U[\rho]$ are known, the ground state energy of the solid can be obtained by variationally minimizing $E[\rho]$ with respect to ρ. Unfortunately, exact expressions for these operators are not known. The Kohn-Sham framework reduces the intractable many-body problem of interacting electrons in a static external potential to a tractable problem of non-interacting electrons moving in an effective potential. Then the functional in Equation 2.11 can be written as a fictitious density functional of a non-interacting system

$$E_{\text{eff}}[\rho] = \langle \Psi_{\text{eff}}[\rho] | T_{\text{eff}} + V_{\text{eff}} | \Psi_{\text{eff}}[\rho] \rangle \tag{2.12}$$

where T_{eff} is the kinetic energy of the non-interacting electrons and V_{eff} is the external effective potential in which they are moving (also known as the Kohn-Sham potential). If this potential is chosen to be

$$V_{\text{eff}} = V + U + (T - T_{\text{eff}}), \tag{2.13}$$

then $\rho_{\text{eff}}(\mathbf{r}) = \rho(\mathbf{r})$. This effective single-electron potential can also be written as

$$V_{\text{eff}}(\mathbf{r}) = V + \int \frac{\rho_{\text{eff}}(\mathbf{r}')}{|\mathbf{r} - \mathbf{r}'|} d^3\mathbf{r}' + V_{\text{XC}}[\rho_{\text{eff}}(\mathbf{r})] \tag{2.14}$$

where the second term describes the electron-electron Coulomb repulsion (also known as the Hartree term) and the last term is the exchange correlation potential that includes all of the many-electron interactions. Although the exact form of the latter is unknown, it can be approximated as a local or nearly local functional of the electron density. Now we can calculate the density of the interacting (many-body) Schrodinger Equation

$$\left[\sum_{i}^{N}\left(-\frac{\hbar^2\nabla_i^2}{2m}+v\left(\mathbf{r}_i\right)\right)+\sum_{i<j}U\left(\mathbf{r}_i,\mathbf{r}_j\right)\right]\Psi\left(\mathbf{r}_1,\mathbf{r}_2,...,\mathbf{r}_N\right)=E\Psi\left(\mathbf{r}_1,\mathbf{r}_2,...,\mathbf{r}_N\right) \tag{2.15}$$

by solving the equations of a noninteracting (single-body) system in a potential V_{eff}

$$\left(-\frac{\hbar^2}{2m}\nabla^2+V_{\text{eff}}(\mathbf{r})\right)\Psi_{\text{eff}}(\mathbf{r})=E_{\text{eff}}\Psi_{\text{eff}}(\mathbf{r}), \tag{2.16}$$

the solution for which can conveniently be written as a single Slater determinant $\Psi = |\psi_1, \psi_2, ..., \psi_N|$ and yields orbitals that reproduce the density of the original system

$$\rho(\mathbf{r})=\sum_{i=1}^{N}|\psi_i(\mathbf{r})|^2, \tag{2.17}$$

where the summation runs over the N orbitals with the lowest eigenvalues [14]. Equations 2.14–2.17 are together referred to a the Kohn-Sham equations. Due to the dependence of the Hartree term and V_{XC} on $\rho(\mathbf{r})$, which depends on ψ_i, which depend on V_{eff}, the Kohn-Sham equations must be solved self-consistently or iteratively until convergence is reached.

2.2.2 Local Density and Generalized Gradient Approximations

The Kohn-Sham equations are exact provided the exchange correlation functional $E_{\text{XC}}[\rho]$ is known, which, of course, is not the case. A number of approximations exist for this term. The simplest is the Local Density Approximation (LDA), which is based on the exact exchange energy for a uniform electron gas. The LDA exchange-

correlation functional is written as

$$E_{\mathrm{XC}}^{\mathrm{LDA}}[\rho] = \int \varepsilon_{\mathrm{XC}}[\rho(\mathbf{r})]\rho(\mathbf{r})d^3\mathbf{r}, \tag{2.18}$$

where $\varepsilon_{\mathrm{XC}}$ is the exchange correlation energy per electron at $\mathbf{r}$ and is set equal to the exchange correlation energy per electron of a homogeneous electron gas with the same density $\rho(\mathbf{r})$ thereby neglecting any non-local effects around $\mathbf{r}$. LDA methods perform surprisingly well for materials with delocalized electrons, e.g. metallic solids, that closely resemble the uniform electron gas, but they tend to run into problems in describing systems with localized electrons [15]. For example, LDA systematically underestimates lattice parameters and band gaps [11]. An improvement on the LDA method is the Generalized Gradient Approximation (GGA), which is still local but also takes into account the gradient of the density at the same coordinate and can be written as

$$E_{\mathrm{XC}}^{\mathrm{GGA}}[\rho_\uparrow, \rho_\downarrow] = \int \varepsilon_{\mathrm{XC}}\left(\rho_\uparrow, \rho_\downarrow, \vec{\nabla}\rho_\uparrow, \vec{\nabla}\rho_\downarrow\right)\rho(\mathbf{r})d^3\mathbf{r}. \tag{2.19}$$

GGA functionals are perhaps the most commonly used in modern DFT calculations. Parameterizations of GGA differ from each other by the choice of $\varepsilon_{\mathrm{XC}}(\rho, \vec{\nabla}\rho)$ and tend to be much more different from each other than various parameterizations of LDA. The GGA parameterization used in all calculations in this work is by Perdew, Burke, and Ernzerhof (PBE) [16, 17].

2.2.3 The Pseudopotential Method

Quite a few numerical techniques exist for the purpose of solving the Kohn-Sham equations, all of them aiming to strike the optimal balance between accuracy and computational efficiency. Among them are the pseudopotential method and the Linear Augmented Plane Wave (LAPW) method, which has been considered the most accurate in past years. The pseudopotential method allows us to replace the influence of the core electrons around the ions that do not strongly affect the bond within a solid with an effective potential. This approximation requires that the pseudo-wave functions of these valence electrons have the same scattering properties as the actual electrons would have and is only valid when the core electrons do not participate in bonding. Because valence wave functions must be orthogonal to core states, they tend to rapidly oscillate near ion cores, which makes them quite difficult to describe. The LAPW method transforms these rapidly oscillating wave functions into smooth ones

that are much more manageable. All of the calculations in this work are performed using the Projector Augmented Wave (PAW) approach, which is a generalization of the pseudopotential and LAPW methods that is relatively accurate and very fast. Lastly, all DFT calculations in this work are performed using the implementation of these methods in the VASP [18, 19, 20, 16, 17, 15, 21].

2.3 Cluster Expansion Formalism

As was previously mentioned, it would, in theory, be nice to calculate all possible excitations of a system with DFT. However, because the number of potential excitations is so large and quantum chemical calculations so expensive, it is more reasonable to invoke a model that would allow us to predict the energies of all excitations by fitting to a finite set of very accurately calculated first principles data. The cluster expansion is a technique for constructing an effective Hamiltonian to predict the energy of a specifically defined system accounting for its various degrees of freedom. While there can be different types of excitations (e.g. vibrational, electronic), in this work, we concern ourselves almost entirely with configurational degrees of freedom. In other words, we look at the properties of a system as a function of its atomic composition and disorder. Because we are primarily dealing with crystalline solids, the lattice, crystallographic sites, and interstitial sites are generally well defined. In an actual solid, the atoms do not occupy the exact lattice sites due to ionic relaxations, but there is, none the less, a one to one correspondence between each atom and a crystallographic site. This setup works equally well for modeling insertion compounds, described in Chapter III, binary alloys (with vacancies), described in Chapter IV, and many other types of systems. Because we are studying configurational disorder, we are interested in how different arrangements of species within a system affect the system's total energy. In a crystal with m sites and two species potentially occupying those sites, there would be a total of 2^m possible arrangements. In the case of insertion compounds, as described in Chapter III, these are arrangements of lithium atoms and vacancies over the interstitial sites of a metal oxide, and in the case of alloys, as in Chapter IV, they are arrangements of different metal atoms over the crystallographic sites of a host lattice. Figure 2.1(a) is an example of an arrangement of two different species on a triangular lattice. At this point, it is useful to define an occupation variable σ_i, which identifies the occupant of a given site i as ± 1. Let's assign $\sigma_i = +1$ for guest atoms (pink) and $\sigma_i = -1$ for host atoms (blue). This assignment is more or less arbitrary, but when we track the composition of this system,

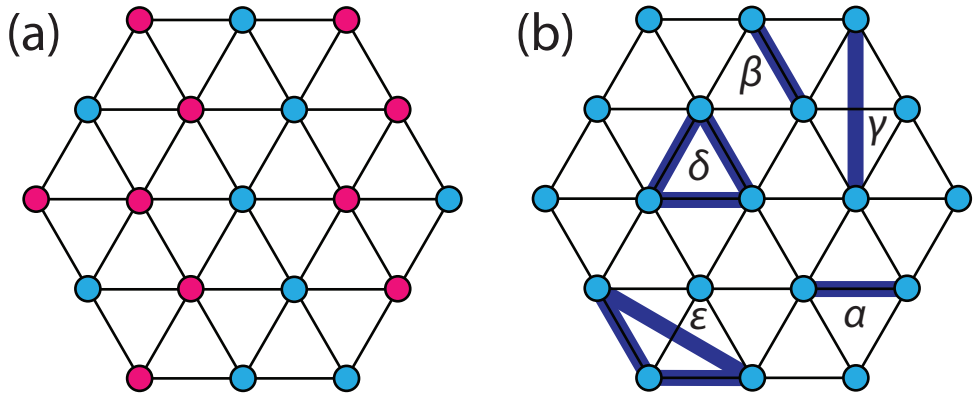

Figure 2.1. An example of how to build a cluster expansion on a triangular lattice. Some arbitrary configuration of pink and blue atoms is shown in (a), and a few example clusters are illustrated in (b).

x will refer to the composition of the species labeled +1. We can then define a vector $\vec{\sigma} = (\sigma_1, \sigma_2, ..., \sigma_i, ..., \sigma_m)$ that uniquely specifies an entire configuration. Additionally, as shown in Figure 2.1(b), we can define clusters of multiple sites (e.g. pairs, triplets, etc.). Then for each cluster, we can write a cluster function as the product of the occupation variables at the cluster sites

$$\phi_\alpha(\vec{\sigma}) = \prod_{i \in \alpha} \sigma_i. \tag{2.20}$$

Equation 2.20 defines ϕ_α specifically for the pair cluster α. If we wanted to evaluate ϕ_α for the configuration in Figure 2.1(a), it would look like

$$\phi_\alpha = \sigma_{\alpha_1} \times \sigma_{\alpha_2} = (-1)(+1) = -1. \tag{2.21}$$

Sanchez *et al* have shown that these cluster functions form a complete orthonormal basis in configuration space and that any property of the system that depends on configuration can be expanded as a linear combination of these functions [22]. This allows us to write the following expression for the energy of a given configuration, which we will refer to as the effective Hamiltonian or Cluster Expansion (CLEX).

$$E(\vec{\sigma}) = V_0 + \sum_\alpha V_\alpha \phi_\alpha(\vec{\sigma}), \tag{2.22}$$

where α indexes the clusters, and V_0 and V_α are the constant expansion coefficients, much like in a Fourier series, and are referred to as Effective Cluster Interactions

(ECI). Alternatively, we can write

$$E(\vec{\sigma}) = V_0 + \sum_i V_i \sigma_i + \sum_{i,j} V_{ij} \sigma_i \sigma_j + \sum_{i,j,k} V_{ijk} \sigma_i \sigma_j \sigma_k, \tag{2.23}$$

where again V are the ECI, linear expansion coefficients, and $i, j, k, ...$ index the individual cluster sites. Equations 2.22 and 2.23 can be thought of as a generalized Ising Hamiltonian that includes not only the nearest neighbor pair interactions but all multibody interactions in the entire infinite crystal. For practical purposes, this expression must be truncated at some point and thus is only useful if it converges quite rapidly, in other words, if there exists a relatively small subset of clusters such that there is a negligible difference between evaluating Equation 2.23 over the entire infinite set of clusters and evaluating it just for this subset.

2.3.1 Determination of Effective Cluster Interaction Coefficients

The cluster expansion Equation 2.23 requires two inputs to evaluate the energy of some specified structure: the unique configuration of host and guest atoms on the lattice and the exact values of the ECI. In some sense, the ECI embody some complex interactions between the host and guest atoms, but it is difficult to assign them any real physical meaning. While Equation 2.22 is exact due to the completeness of the crystal basis, the cluster expansion can be truncated to include only a few terms, usually those corresponding to relatively small clusters (containing no more than four or five sites). Then, to determine the ECI, we perform a least squares fit to some set of formation energies calculated from first principles with DFT. Due to the crystal's factor group symmetry, addressed in detail in Appendix A, and translational periodicity, only a small portion of the ECI are actually linearly independent. The quality of the parametrization, as well as where it will be truncated, is evaluated using two metrics: Root Mean Square (RMS) error, which measures the reproducibility of the formation energies, and the Cross-Validation (CV) score, which measures the degree of predictability of the fit [23]. The leave-one-out CV score is calculated as follows.

$$CV^2 = \frac{1}{N} \sum_{i=1}^{N} \left(E(\vec{\sigma}_i) - E'(\vec{\sigma}_i)^2 \right), \tag{2.24}$$

where $E(\vec{\sigma}_i)$ is the first principles (DFT-calculated) energy of the configuration i, $E'(\vec{\sigma}_i)$ is the predicted value of $E(\vec{\sigma}_i)$ obtained by performing a least-squares fit to

the data from the other $N-1$ configurations (not including $\vec{\sigma}_i$), and then evaluating the resulting expansion at $\vec{\sigma}_i$. The optimal set of crystal basis functions ϕ to describe the system will minimize the CV score. We use a collection of genetic algorithm and depth-first-search techniques to achieve this minimization [24].

Additionally, some qualitative considerations go into choosing the most suitable fit parameters. For example, even in a scenario with favorable RMS and CV values (thought this is unlikely), an expansion that predicts some configuration to be stable while that structure is determined by first principles methods to be unstable or metastable.

2.4 Grand Canonical Monte Carlo Simulations

Monte Carlo simulations are a tool used in statistical mechanics to sample different microstates of the system and calculate thermodynamic averages. The sampling frequency is related to the probability distribution function (Equation 2.1). We specifically employ the Metropolis algorithm, which starts with an arbitrary configuration and proceeds to visit a sequence of successive states of a Markov chain [25]. The transition probability from the current configuration A to the next configuration B is then given by the following rule

$$P(A \rightarrow B) = \begin{cases} 1 & \text{if} \quad \Omega_B < \Omega_A \\ e^{-\Delta\Omega/k_B T} & \text{if} \quad \Omega_B \geq \Omega_A \end{cases}, \tag{2.25}$$

where $\Delta\Omega = \Omega_B - \Omega_A$ is the difference in energy between the two states, k_B is the Boltzmann constant, and T is the temperature. Here, Ω is the grand canonical energy and is generally defined as

$$\Omega = E\left(\vec{\sigma}\right) - \mu N, \tag{2.26}$$

where $E\left(\vec{\sigma}\right)$ is the average energy, μ is the chemical potential, and N is the number of atoms. If the transition probability $P(A \rightarrow B)$ is greater than a randomly generated number, the new configuration σ_B is accepted; otherwise, the system remains in state σ_A.

Upon convergence, the metropolis algorithm will sample configurations within the simulation according to the probability distribution function (Equation 2.1), which allows us to simply average arithmetically over the configurations to obtain the thermodynamic averages in Equation 2.3. The primary reason for constructing a cluster

expansion effective Hamiltonian for our system is to allow for the rapid and accurate estimation of the formation energy of any imaginable configuration. We can employ this tool in a Monte Carlo simulation to sample a very large number of the system's microstates in an attempt to predict its finite temperature thermodynamic properties. Typically 3,000-10,000 Monte Carlo passes are required for reasonable averaging in a single simulation. The first several hundred (usually up to 1,000) passes are for equilibration of the system and are not included in the averaging. We specifically employ two different types of Monte Carlo simulations: (1) heating and cooling runs at constant chemical potential and (2) chemical potential runs at constant temperature. Both of these allow for the determination of phase boundaries and construction of phase diagrams, and (2) specifically yields the voltage curve for lithium insertion processes.

2.5 Lattice Model Diffusion and Transition State Theory

The atoms on a crystal lattice, for example, lithium ions in the interstitial sites of anatase TiO_2, spend the majority of their time around their well defined equilibrium sites. Occasionally, however, they travel along the possible paths connecting adjacent sites (when the destination site is vacant), which results in diffusion. Transition state theory serves as a very good approximation for the frequency with which ions move between neighboring sites. The diffusion coefficient depends on both the thermodynamic and kinetic properties of the solid. It is convenient to write [26]

$$D = \Theta D_J \tag{2.27}$$

where D_J is the self diffusion coefficient and Θ is the thermodynamic factor, which is defined as

$$\Theta = \frac{1}{k_B T} \frac{\partial \mu_{\mathrm{Li}}}{\partial \ln x}. \tag{2.28}$$

This quantity measures the deviation from thermodynamic ideality: Θ is equal to 1 in the dilute limit and diverges near ordered phases, which do not at all behave like ideal solutions. The self diffusion coefficients are determined by evaluating Kubo-Green expressions within kinetic Monte Carlo simulations.

$$D_J = \frac{1}{2dt} \left\langle \frac{1}{N} \left(\sum_{i=1}^{N} \Delta \vec{R}_i(t) \right)^2 \right\rangle, \tag{2.29}$$

where d is the dimension of the lattice, N is the number of lithium ions, and $\Delta\vec{R}_i(t)$ is a vector connecting the end points of the trajectory of a particular ion i at time t. The angle brackets denote a statistical mechanical ensemble average. Similarly, the tracer diffusion coefficient is defined as

$$D^* = \frac{1}{2dt}\frac{1}{N}\sum_{i=1}^{N}\left\langle \left(\Delta\vec{R}_i(t)\right)^2 \right\rangle. \tag{2.30}$$

The self diffusion coefficient is related to the square of the displacement of the center of mass of all migrating atoms at equilibrium. The tracer diffusion coefficient, however, is related to square of the displacement of just one atom and thus measures the mobility of individual atoms. Trajectories are simulated in kinetic Monte Carlo simulations using transition state theory to estimate hop frequencies for elementary hops. According to transition state theory, the hop frequency can be written as

$$\Gamma = \nu^* e^{\frac{\Delta E}{kT}}, \tag{2.31}$$

where ΔE is the migration barrier for a particular hop, k is the Boltzmann constant, and T is the temperature. The vibrational prefactor, ν^*, must be determined for each specific system under study. In Chapter III, it is chosen to be 10^{13} Hz, a typical value for titanates[27].

The migration barrier ΔE is calculated from first principles with DFT using the Nudged Elastic Band (NEB) method. In order to accurately describe diffusion in a real system, however, we must consider all possible symmetrically unique migration paths in a crystal as well as the effect of the local environment on the activation barriers. It is convenient to introduce here a Kinetically Resolved Activation Barrier (KRA), which allows us to correctly treat the migration barriers of forward and backward hops in the simulation. If needed, the dependence of the ΔE_{KRA} on the surrounding atomic configuration can be treated with a local cluster expansion [28].

2.5.1 Kinetic Monte Carlo

Kinetic Monte Carlo (KMC) simulations are a powerful tool in the investigation of the transport properties of a system, e.g. chemical diffusion coefficients. In the KMC algorithm, we are able to simulate the migration of multiple ions within a host. Individual hops occur with the probability given by the hop frequency in Equation 2.31.

For a fixed temperature and composition, the KMC simulation begins with some predetermined configuration (typically a ground state structure from grand canonical

Monte Carlo). All possible migration probabilities Γ_m are determined for the paths available to the diffusing ions. The destination site for any moving ion must be vacant in order for the transition to be possible (and thus have a nonzero transition probability). The chance that any given event will occur is given by $\Gamma_m/\Gamma_{\mathrm{tot}}$, where Γ_{tot} is the sum of all individual probabilities Γ_m. Then the time is updated according to

$$\Delta t = -\frac{\log \zeta}{\Gamma_{\mathrm{tot}}} \tag{2.32}$$

where ζ is a random number between 0 and 1. This constitutes a single kinetic Monte Carlo step and is repeated as many times as there are migrating atoms in the simulation. Similarly to the grand canonical simulations described in Section 2.4, a number of equilibration steps are performed before averaging for D_J and D^* begins over the course of several thousand passes.

CHAPTER III

Kinetics of Anatase TiO_2 Electrodes: the Role of Ordering, Anisotropy, and Shape Memory Effects

3.1 Introduction

Lithium-ion battery materials are remarkable in their ability to undergo large variations in Li concentration at room temperature. This phenomenon requires large open spaces, a low susceptibility to dramatic phase transitions, and high ion mobilities. Anatase TiO_2 has been extensively studied over the past decades due to its potential applications in photovoltaic[29, 30], electrochromic[30], and electrochemical[29, 31, 32, 33, 34, 35, 36] devices, showing promise as a viable electrode material for Li-batteries.

Anatase has a tetragonal unit cell that can theoretically accommodate one lithium for every titanium. Upon lithiation to $Li_{0.5}TiO_2$, anatase is observed to undergo a tetragonal to orthorhombic phase transition. This composition is also most frequently reported as the maximum electrochemical insertion limit of Li into bulk anatase, although concentrations as high as 0.6 have been reported[32, 37, 38]. Only with nanostructured anatase TiO_2 has the theoretical capacity of $x = 1.0$ been reached[39]. It has been suggested that the limited capacity of bulk anatase is due to a low Li diffusion coefficient in the fully lithiated phase[39, 40]. Here, we discuss a first-principles study of the thermodynamic and kinetic properties of lithiated anatase TiO_2 and provide crucial insight about the role of electronic and crystallographic properties of anatase TiO_2 in limiting the achievable capacity to slightly more than half of its theoretical value. We find that the thermodynamically stable ordered phase at $x = 0.5$ can accommodate excess Li over vacant sites up to $x = 0.6$ and that Li diffusion in this phase is strictly one dimensional at room temperature with a diffusion coefficient that is lower than that of Li diffusion in anatase TiO_2. We also predict

that the Li diffusion coefficient in the fully lithiated phase, $LiTiO_2$, is several orders of magnitude lower than that in TiO_2 and $Li_{0.5}TiO_2$ due to the absence of distorted Ti-O octahedra that open up the Li diffusion path in dilute TiO_2. We argue that this is responsible for capping the achievable capacity of anatase TiO_2 to approximately half of its theoretical value in bulk crystallites.

Our analysis also points to a strong coupling between kinetic behavior and electrode particle shape, providing new insights as to how morphology can be exploited to enhance charge and discharge rates and minimize hysteresis. The dimensional changes accompanying the tetragonal TiO_2 to orthorhombic $Li_{0.5}TiO_2$ transition satisfy conditions for a strain invariant interface separating the two phases when they coexist in the same particle. The transformation therefore should have much in common with those occurring in shape memory alloys. The predicted one-dimensional diffusion direction in $Li_{0.5}TiO_2$, however, is parallel to the strain invariant interface and has no component towards those interfaces. This suggests that large, coarse particle morphologies that are susceptible to a core-shell two-phase mechanism will lead to limited capacity and rates.

3.2 Methods

We used a combination of first principles total energy calculations and statistical mechanics techniques to study phase stability and transport properties in lithiated anatase TiO_2.

3.2.1 Total Energy Calculations

The first principles calculations in this work were performed using DFT within GGA as implemented in the VASP code. We use the PAW pseudopotential method to treat the interaction between valence and core electronic states. The calculations were done non-magnetically because the inclusion of spin polarization had a negligible effect on the energy. The atomic positions, lattice parameters, and cell shape were allowed to relax fully using the conjugate gradient approach to minimize the total energy. We used a $12 \times 12 \times 6$ k-point mesh for the tetragonal anatase unit cell to ensure that the energies converge to within 2.5 meV per TiO_2 formula unit, and an energy cutoff of 400 eV was chosen for our plane wave basis set. We calculated the energies of 188 different Li-vacancy configurations over the octahedral sites of the anatase TiO_2 host crystal. The k-point meshes for supercell configurations were chosen to have a reciprocal space density equivalent to (or greater than) that for the

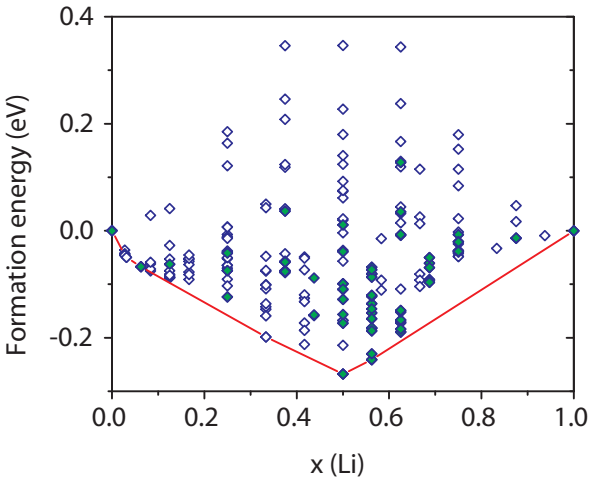

Figure 3.1. DFT formation energies for Li_xTiO as calculated with VASP for 188 different Li-vacancy configurations over the octahedral sites of anatase. The red line represents the convex hull. The points included in the cluster expansion fit are shaded green.

tetragonal unit cell of anatase TiO_2. The VASP calculated formation energies are shown in Figure 3.1.

3.2.2 Cluster Expansions

We used the cluster expansion formalism to extrapolate the DFT formation energies to arbitrary Li-vacancy configurations over the octahedral interstitial sites of anatase TiO_2 within Monte Carlo simulations. The addition of Li to the anatase TiO_2 host leads to large relaxations, with a gradual loss of distortions of the TiO_6 octahedra as the Li concentration increases. The bond lengths and angles in the orthorhombic ground state of $Li_{0.5}TiO_2$ are significantly different from those in the tetragonal end states at $x = 0$ and $x = 1$. Additionally, the non-linear variation of the formation energies at dilute Li concentrations suggests important non-local, long-range interactions. Strong concentration dependent relaxations and non-local interactions make it difficult to construct a rapidly convergent real space cluster expansion for the configurational energy of the anatase Li_xTiO_2 system over the entire composition range. However, for the purpose of studying phase stability and other thermodynamic properties at finite temperature, it is not necessary to work with a cluster expansion that is accurate over the whole Li concentration interval between 0 and 1. Indeed, the formation energies of Figure 3.1 suggest that the low to intermediate temperature-composition phase diagram will contain two two-phase regions: one between dilute Li_xTiO_2 and $Li_{0.5}TiO_2$ and another between $Li_{0.5+y}TiO_2$ and $LiTiO_2$. Predicting thermodynamic properties and phase stability at room temperature is

therefore possible by considering the configurational excitations that are only small perturbations of the ground state structures. To this end, we separately constructed a cluster expansion that accurately describes the energy of configurational excitations within the $Li_{0.5}TiO_2$ ground state and for dilute Li_xTiO_2. We point out that an ordered phase at $x = 1/3$ is predicted to be marginally stable at zero Kelvin as it appears on the convex hull in Figure 3.1. We found, however, that at room temperature, this ordered phase at $x = 1/3$ (neglecting configurational excitations within this phase) is no longer stable relative to the room temperature free energies for α-Li_xTiO_2 and β-$Li_{0.5}TiO_2$, as calculated with Monte Carlo simulations that are described below. For clarity, will henceforth refer to the $Li_{0.5}TiO_2$ ordered phase as β, using α to denote anatase TiO_2, and γ to denote fully lithiated anatase, $LiTiO_2$.

The β-$Li_{0.5}TiO_2$ ground state consists of a lithium sublattice and a vacancy sublattice. Configurational excitations within this ground state involve the introduction of vacancies on the Li sublattice or of Li on the vacancy sublattice. To describe these configurational degrees of freedom, we introduce occupation variables, σ_i, for the vacancy sublattice, which are $+1$ if the site i is occupied by Li and 0 if site i is vacant, and occupation variables σ_j for the Li sublattice, which are $+1$ if site j is vacant and 0 if site j is occupied by Li. The configurational energy then takes the form

$$E(\sigma_1, ..., \sigma_i, ..., \sigma_M, \delta_1, ..., \delta_j, ...\delta_M) = V_0 + \sum_{\delta} V_\delta \cdot \Phi_\delta + \sum_{\gamma} V_\gamma \cdot \Phi_\gamma + \sum_{\lambda} V_\lambda \cdot \Phi_\lambda, \tag{3.1}$$

where the cluster functions

$$\Phi_\delta = \prod_{i \in \delta} \sigma_i, \qquad \Phi_\gamma = \prod_{j \in \gamma} \delta_j, \qquad \Phi_\lambda = \prod_{k,l \in \lambda} \sigma_k \cdot \delta_l \tag{3.2}$$

are products of occupation variables belonging to clusters of sites. Here, δ indexes clusters of sites on the vacancy sublattice, γ indexes clusters of sites on the Li-sublattice, and λ indexes clusters containing sites from both sublattices. All configurations in the anatase system are accessible with this description; however, the cluster expansion formulated here conveniently describes the energy of small configurational perturbations relative to the ground state at $x = 0.5$. With the particular choice of occupation variables introduced here, the energy of the unperturbed ground state at $x = 0.5$ is equal to V_0 because all of the occupation variables in the perfectly ordered $Li_{0.5}TiO_2$ ground state are 0. The fit of the coefficients V_ε (with $\varepsilon = \delta, \gamma$, or λ) of the above cluster expansion for β-$Li_{0.5}TiO_2$ includes a total of 14 non-zero terms

corresponding to the empty cluster V_0, 2 point clusters (one for each sublattice), 8 pair clusters, and 3 triplet clusters. The coefficients were fit to 25 DFT formation energies for Li-vacancy configurations that deviated slightly from the perfectly ordered β-$Li_{0.5}TiO_2$ configuration. For this fit, the RMS is 0.005 eV per TiO_2 formula unit and the CV score is 0.015 eV per TiO_2 formula unit.

We also constructed a cluster expansion in the dilute limit. In this case, we only have one sublattice corresponding to all of the possible octahedral sites that lithium is allowed to occupy in anatase. The formation energies in the dilute limit show a strong concentration dependence, implying that non-local interactions that are difficult to capture with a truncated cluster expansion are important. Hence, we supplemented a truncated cluster expansion with a polynomial that depends only on the overall concentration.

$$E\left(\vec{\sigma}\right) = V_0 + \sum_{\alpha} V_\alpha \cdot \Phi_\alpha\left(\vec{\sigma}\right) + f(x) \tag{3.3}$$

$$f(x) = x(x-1)\sum_{n=0}^{\infty} L_n(2x-1)^n \tag{3.4}$$

The coefficients in this energy expansion were fit to 97 DFT formation energies, most for Li-vacancy configurations having a dilute concentration. For this fit, the RMS is 0.013 eV per TiO_2 formula unit and the CV score is 0.017 eV per TiO_2 formula unit.

3.2.3 Grand Canonical Monte Carlo

The above cluster expansions were used in grand canonical Monte Carlo simulations to calculate finite temperature thermodynamic properties. Free energies and voltage curves were determined as described by Dalton *et al*[41]. We used a $12\times6\times6$ supercell of the $Li_{0.5}TiO_2$ unit cell and for each temperature and chemical potential performed 6,000 Monte Carlo passes (i.e. each Li site visited on average 6,000 times). The first 3,000 Monte Carlo passes were equilibration steps after which averaging was performed. For dilute lithium compositions, the input conditions are the same except that a $12 \times 12 \times 12$ supercell of the tetragonal anatase unit cell is used. Thus, all Monte Carlo cells are the same size.

3.2.4 Diffusion Activation Barriers

The activation barriers for Li hops into adjacent vacant sites, ΔE, for anatase, $Li_{0.5}TiO_2$, and $LiTiO_2$ were calculated using the NEB method as implemented in

VASP. All barrier calculations were performed at constant volume in a $2 \times 2 \times 1$ supercell containing 16 titanium atoms and 32 oxygen atoms, using the relaxed pure anatase ground state cell volume. The dilute calculations included a single Li atom, the hopping atom. The β-$Li_{0.5}TiO_2$ calculations included the 8 Li atoms that form the sublattice ordering (with one of them performing the hop) $\pm$ 1 Li in the cases that incorporate defects, for example, an extra Li or vacancy. We also performed the dilute NEB calculations in larger supercells ($2\sqrt{2} \times 2\sqrt{2} \times 1$, containing 32 Ti atoms and 64 O atoms, and $3 \times 3 \times 1$, containing 36 Ti atoms and 72 O atoms) to determine if the supercell size had an effect on the activation barrier. In each of these cases, only one Li atom, the hopping atom, is present in the crystal, and the lattice parameters are constrained to those of pure anatase TiO_2. The resulting diffusion barriers in order of increasing supercell size were 0.500 eV, 0.494 eV, and 0.515 eV, respectively, allowing us to conclude that the use of a $2 \times 2 \times 1$ supercell is, indeed, sufficient in this context.

Migration barriers were calculated for 9 different hops in various local environments in the ordered β-Li_xTiO_2 phase. These included hops in the perfectly ordered phase and in configurations that were slightly sub- or over-stoichiometric. For all 9 hops, we found that the KRA, an effective barrier averaged over the forward and backward hops[28], falls into two categories: a low value around 0.56 eV for hops between Li sites that are close together (hop I in Figure 3.2(b)) and a high value of 1.25 eV for hops connecting Li sites that are farther apart (hop II in Figure 3.2(b)).

3.2.5 Kinetic Monte Carlo

The kinetic Monte Carlo cells had the same dimensions as used in grand canonical Monte Carlo. At each Li concentration, we averaged over 200 initial starting configurations and for each of these performed 2000 Monte Carlo passes with the first 1000 passes being equilibration steps.

3.3 Results and Discussion

We performed a comprehensive study of phase stability using the cluster expansion formalism[22] as implemented in the CASM code[42]. As a first step, we enumerated a large number of Li-vacancy configurations over the octahedral sites of anatase TiO_2, calculating the energies of 188 of them with the VASP code[18, 20, 21]. The calculated formation energies confirm the stability of the ordered phase at $x = 0.5$, predicted by Morgan[43] with similarities to that postulated by Wagemaker[44]. This

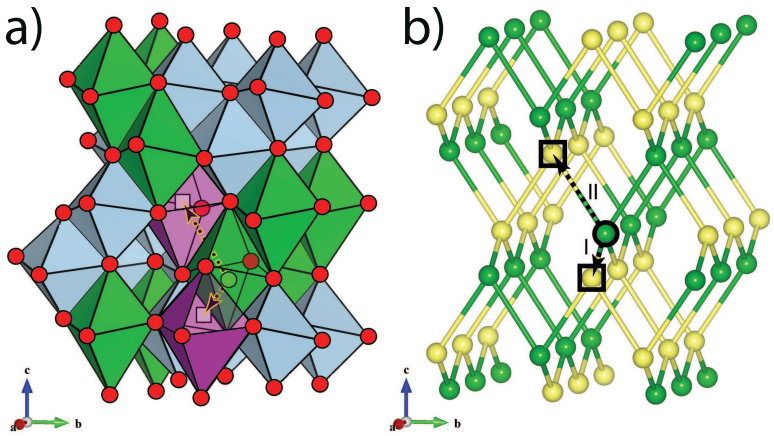

Figure 3.2. The lithium-vacancy ordering of the β-$Li_{0.5}TiO_2$ phase. In a), the lithium, titanium, and vacancy octahedra are green, blue, and purple, respectively. In b), only the lithium (green) and vacancy (yellow) sublattices are shown. The arrows indicate possible diffusion hop paths.

phase is responsible for the step in the voltage vs. lithium composition curve. The ordered phase is characterized by a zig-zag arrangement of Li and vacancies causing an expansion along the b-axis and a contraction along the c-axis of the anatase host with little change in the a lattice parameter. These dimensional changes break the tetragonal symmetry of the anatase host, reducing it to an orthorhombic space group. The predicted lattice parameters of the ordering at $x = 0.5$ are: $a = 3.81$ Å, $b = 8.21$ Å, $c = 9.20$ Å (anatase: $a = b = 3.81$ Å, $c = 9.68$ Å), which are in good agreement with experimental neutron diffraction measurements by Cava[45, 46]. The unique lithium-vacancy ordering of this structure results in a larger primitive unit cell (doubling of the original a-axis of anatase along the b direction) and places it in the *Pnnm* (#58) space group, as illustrated in Figure 3.2. The structure's Wyckoff positions are reported in Table 3.1. We will refer to this ordered phase as β, using α to denote anatase TiO_2, potentially having a dilute Li concentration, and γ to denote fully lithiated anatase, $LiTiO_2$.

The first-principles formation energies of the 188 Li-vacancy configurations were used to construct cluster expansions for the configurational energy: one for the dilute limit and a second to describe the energy of β-Li_xTiO_2 as a function of configurational excitations relative to its perfectly ordered state at $x = 0.5$. The cluster expansions were implemented in Monte Carlo simulations to calculate free energies and chemical potentials as a function of Li concentration. The voltage is related to minus the Li chemical potential according to the Nernst equation. Figure 3.3 shows the predicted voltage vs. lithium composition curve at room temperature (300 K). It is character-

Atom	Position	x	y	z
Li	$4g$	0.66511	0.12360	0.50000
Ti	$4g$	0.60639	0.38293	0.00000
Ti	$4g$	0.88519	0.36215	0.50000
O	$4g$	0.65146	0.36558	0.50000
O	$4g$	0.84361	0.38313	0.00000
O	$4g$	0.59474	0.12376	0.00000
O	$4g$	0.88727	0.12558	0.50000

Table 3.1. The Wyckoff table for β-$Li_{0.5}TiO_2$, including Wyckoff positions and fractional coordinates for atoms in the asymmetric unit of the β-$Li_{0.5}TiO_2$ ordered phase structure.

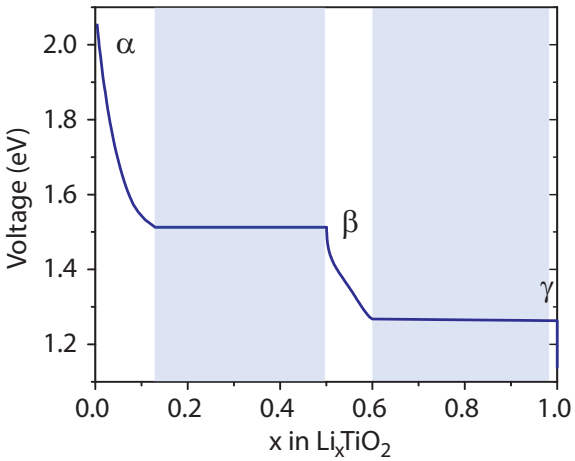

Figure 3.3. The calculated voltage vs. lithium composition curve for Li_xTiO_2 at 300 K was obtained using grand canonical Monte Carlo simulations with a cluster expansion. The blue shading indicates two phase regions.

ized by two large plateaus separated by a step around $x = 0.5$. The step between $x = 0.5$ and 0.58 emerges from the stability of β-Li_xTiO_2. Monte Carlo simulations reveal that ordered β-$Li_{0.5}TiO_2$ can easily accommodate additional Li over its vacant sites up to a composition of $x = 0.58$. In contrast, removal of Li from the Li sublattice in β-$Li_{0.5}TiO_2$ results in a large energy penalty, thereby limiting the stability of β-Li_xTiO_2 between 0.5 and 0.58. The first plateau arises from a two-phase coexistence between α-$Li_0.1TiO_2$ and β-$Li_{0.5}TiO_2$, and the second plateau is due to a two-phase coexistence between β-$Li_{0.58}TiO_2$ and γ-$Li_{1.0}TiO_2$. The prediction that the second plateau is well above zero volts indicates that the limit in achievable capacity is not thermodynamic in origin but rather kinetic. For most insertion compounds, voltage vs. lithium composition curves predicted with methods relying on approximations to DFT are systematically underpredicted. For example, the first plateau is predicted to occur at 1.5 V, while experimentally it is measured around 1.78 V[34].

In order to elucidate the behavior of anatase during charge and discharge, we investigated the mechanisms with which Li ions diffuse within the α, β, and γ forms of anatase Li_xTiO_2. We used the NEB method as implemented in VASP to calculate the activation barriers for a large number of possible diffusion hops in α-, β- and γ-Li_xTiO_2 and KMC simulations to calculate macroscopic diffusion coefficients as described elsewhere[27, 42].

In α-Li_xTiO_2, where the Li concentration is dilute, all of the available sites are equivalent, and all hops into adjacent vacancies are symmetrically identical. Lithium ions occupying octahedral sites within transition metal oxide and sulfide insertion compounds typically perform curved hops, passing through an adjacent tetrahedral site[42, 47]. In anatase, however, the adjacent tetrahedral sites between neighboring Li-octahedra share faces with two Ti containing octahedra. The strong electrostatic repulsion from these face-sharing Ti renders the tetrahedral sites unstable, forcing Li to pass through more constricted octahedron edges, whereby it has to squeeze between two edge-forming oxygen atoms, as illustrated in Figure 3.4. The octahedral sites that can accommodate lithium in anatase TiO_2 are noticeably distorted due to the presence of Ti^{4+} with edge lengths (O-O interatomic distance) varying between 3.08 Å and 3.77 Å. In the fully lithiated γ-$LiTiO_2$, in contrast, the octahedral distortions are absent due to the change in the effective Ti valence from 4+ to 3+ upon addition of Li to anatase TiO_2. The edge lengths of the octahedra are now uniform and noticeably smaller at 2.96 Å. This change in edge length with Li concentration has important consequences for the Li migration barriers. Calculated migration barriers in dilute anatase and in fully lithiated anatase (containing one vacancy) are shown

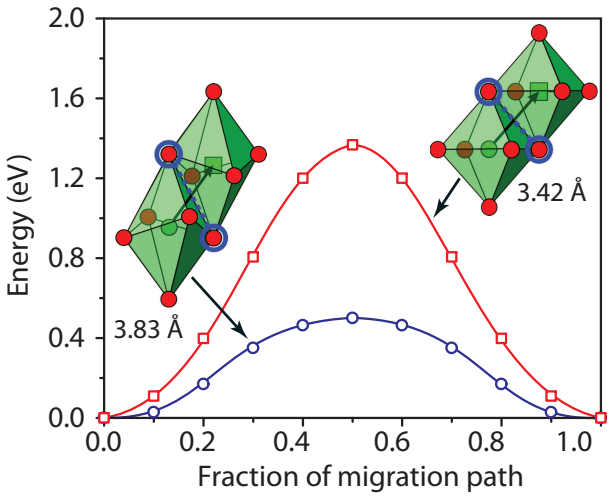

Figure 3.4. Minimal energy migration paths in the dilute α phase (blue circles) and fully lithiated γ phase (red squares) are calculated with the nudged elastic band method in VASP.

in Figure 3.4, from which it is clear that as the octahedral distortions disappear with increasing Li concentration, creating more uniform edges, it becomes more difficult for a diffusing atom to pass between the two oxygen atoms that form the octahedron edge. This results in the much higher barrier of 1.37 eV for a hop in γ-$LiTiO_2$ than a corresponding 0.50 eV barrier in dilute α-Li_xTiO_2, in which the octahedral distortions separate the pair of oxygen ions adjacent to the activated state. This large difference in migration barrier leads to an astounding 14 orders of magnitude drop in the chemical diffusion coefficient when going from dilute anatase to fully lithiated anatase.

Each Li within the zigzag ordering of β-Li_xTiO_2 is coordinated by one other lithium atom and three vacant sites, two of which are symmetrically equivalent. As a consequence, two symmetrically distinct hops of lithium atoms into adjacent vacant sites are now allowed, as shown in Figure 3.2. An atom hopping along path II travels 3.68 Å in the a-c plane while an atom hopping along path I only travels 2.46 Å in the b-c plane. These large differences in hop distances are correlated with large differences in migration barriers, with an activation barrier of 1.55 eV along the long path II, which is much higher than the barrier along the short path I of only 0.78 eV, as shown in Figure 3.5. Similar trends were found for Li hops within β-Li_xTiO_2 after the introduction of local disorder due, for example, to slight deviations from stoichiometry. Such a dramatic difference in activation barriers for the two hop paths suggests the possibility of one-dimensional diffusion along the a-axis in β-Li_xTiO_2.

We used our cluster expansion in combination with KMC simulations as imple-

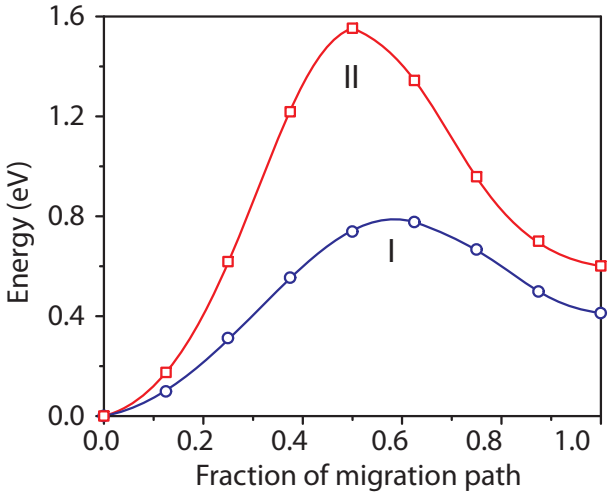

Figure 3.5. Minimal energy migration path for the two symmetrically distinct hops available to a diffusing lithium atom in β-$Li_{0.5}TiO_2$. The barrier for hop a (blue circles) is much smaller than the barrier for hop b (red squares).

mented in the CASM code to calculate the diffusion coefficients for lithium atoms in Li_xTiO_2 at different lithium compositions. The diffusion coefficient, D, appearing in Fick's first law can be written as a product of a thermodynamic factor, Θ, and a kinetic factor, D_J, referred to as a self or intrinsic diffusion coefficient[26]. The thermodynamic factor measures the deviation from thermodynamic ideality and is related to the derivative of the Li chemical potential with respect to the natural log of the Li concentration. The self diffusion coefficient can be calculated with KMC by evaluating a Kubo-Green expression[26]. A more detailed explanation of these concepts and methods is available elsewhere[48].

Figure 3.6 shows the chemical diffusion coefficient as a function of Li concentration. The diffusion coefficient is slightly anisotropic in α and γ (the difference is not discernable on the logarithmic scale of Figure 3.6). In the β phase, extensive KMC simulations at 300 K showed that 100% of the hops occurred along path I, implying that hops along path II are negligible at room temperature and diffusion in the ordered β phase is one-dimensional (along the a-axis). At low concentration, D is comparable to that of other insertion compounds. Our predicted value of 10^{-10} cm^2/s is likely an upper bound as we neglect interactions between Li and localized electronic states, which tend to reduce Li mobility especially at dilute concentrations[49]. D drops substantially at $x = 0.5$ to about 10^{-16} cm^2/s. In the fully lithiated phase, $LiTiO_2$, the absence of distorted Ti-O octahedra results in an even larger drop in the chemical diffusion coefficient to a value of 10^{-24} cm^2/s.

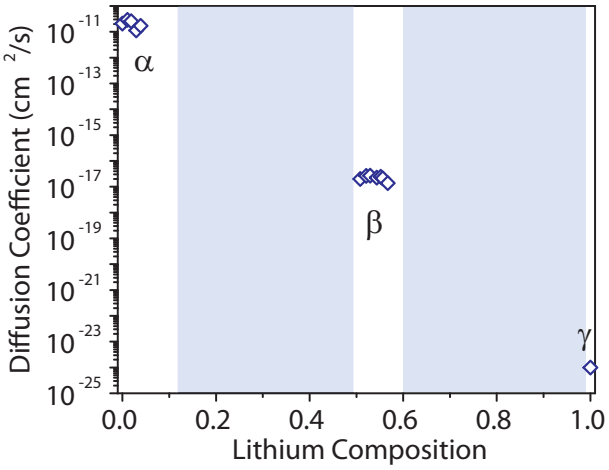

Figure 3.6. The chemical (blue diamonds) diffusion coefficient in the a direction is plotted as a function of lithium concentration at 300 K. The blue shading indicates two phase regions.

Our thermodynamic and kinetic predictions provide crucial insight to rationalize and overcome the cycling and capacity limitations of anatase. One key prediction is the very low Li diffusion coefficient in the fully lithiated phase, which explains the limited capacity of anatase electrodes. Our thermodynamic predictions indicate that fully lithiated γ-$LiTiO_2$ should form through a two-phase reaction from β-$Li_{0.58}TiO_2$. One mechanism for such a reaction is with a core-shell morphology where the new, Li-rich, γ-$LiTiO_2$ phase forms on the surface of the electrode particles and grows inward consuming the β-$Li_{0.58}TiO_2$ as Li is supplied to the particle. In order for Li to reach the two-phase reaction front, however, it must diffuse through γ-$LiTiO_2$, which has enveloped the surface. The exceedingly low Li diffusion coefficient in γ-$LiTiO_2$ will prevent any substantial ingress of Li once a thin layer of γ-$LiTiO_2$ covers the particle surface. This effectively limits the maximum Li concentration of anatase to the solubility limit of β-$Li_{0.5}TiO_2$, which our thermodynamic analysis indicates is about 0.6, in excellent agreement with practically achievable capacities in anatase [32, 37, 38]. Only for the smallest nanoparticles of anatase can we expect higher Li concentrations, when diffusion distances are so small that diffusion is no longer rate-limiting[50, 51]. In this context, Borghols *et al* were able to show that smaller nanoparticles of anatase can be lithiated more successfully than larger ones. In fact, 7 nm nanoparticles can be fully lithiated to $x = 1.0$[39]. Similarly, Bresser *et al* have reported capacities up to $x = 0.75$ for 3-4 nm diameter anatase nanorods[52].

Our results also shed light on the α-TiO_2 to β-$Li_{0.5}TiO_2$ two-phase reaction, which has been studied extensively experimentally[38, 45, 46]. While the a-axis of anatase

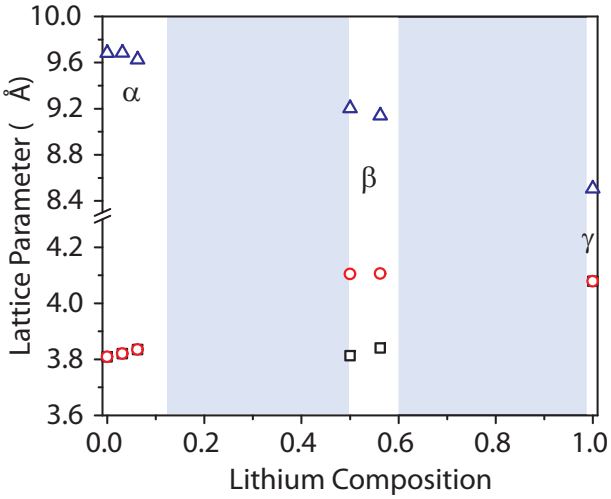

Figure 3.7. Trend in the lattice parameters of Li_xTiO_2 as a function of lithium composition for the structures on the convex hull in Figure 3.1.

(α-TiO_2) and of β-$Li_{0.5}TiO_2$ have negligible misfit (0.1%), the c-axis contracts by 5.0%, and the b-axis expands by 7.7% when transforming from α-TiO_2 to β-$Li_{0.5}TiO_2$ (lattice parameter trends can be seen in Figure 3.7). Within a two-phase reaction model, characterized by a transient two-phase coexistence within each individual particle, such a large lattice misfit typically results in significant coherency strain energies[53]. Unique to this particular two-phase reaction, however, is that the misfit strains are restricted to the b-c plane of β-$Li_{0.5}TiO_2$, with contraction along c and expansion along b. As is well known from the study of martensitic transformations in metallurgy, this condition results in planes that are common to both α-TiO_2 and β-$Li_{0.5}TiO_2$ with zero misfit strain[54]. Two-phase morphologies within single particles are therefore possible without introducing coherency strains, provided that the interface between α and β is parallel to any of the strain invariant planes. For the tetragonal to orthorhombic transformation between α and β, the strain free interfaces will be parallel to the (0, 0.207, $\pm$0.064) and (0.207, 0, $\pm$0.064) habit planes[53]. Because the strain invariant planes in β are perpendicular to the b-c plane, and therefore parallel to the a-axis (the direction of Li diffusion in β) Li diffusion in β can only occur parallel to the reaction front and not toward it. Hence, diffusion through newly formed β is unlikely to contribute to its further growth. Instead, Li must be supplied from the α-TiO_2 side of the reaction front, as illustrated in Figure 3.8. This is only possible if the α phase extends to the surface of the particle throughout the two-phase reaction to allow additional Li to enter the crystal. Any particle shapes that promote a core-shell growth mechanism, with β covering the whole particle, are

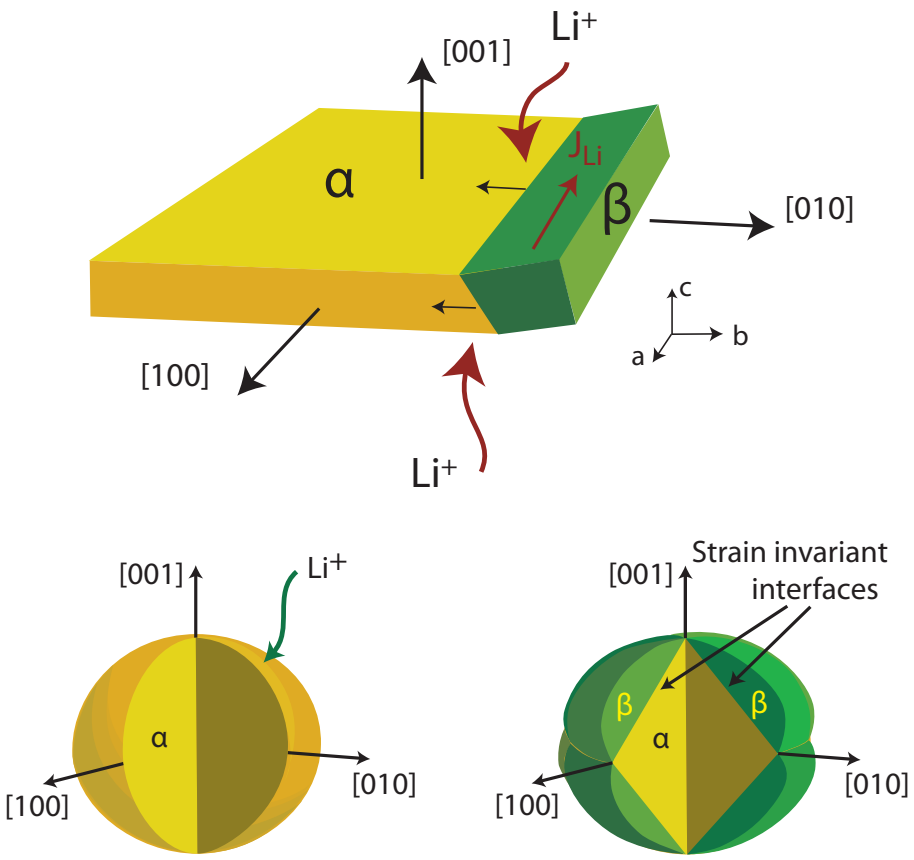

Figure 3.8. The strain-invariant interface between α and β is parallel to the 1-dimensional lithium diffusion direction in β. A two-phase reaction will require Li addition through the original α phase, which is more likely in plate-like particles (a) than in large coarse particles (b) that are more susceptible to a core-shell-mechanism.

undesirable as they would rapidly cut off the Li supply to the moving interface. To ensure full completion of the two-phase reaction, the moving interface must extend to the surface of the particle (Figure 3.8(a)) such that fresh α-TiO_2 surface is always exposed to enable additional Li to enter the crystal. This is more likely in plate-like particles that are thin in the [001] direction.

For large anatase particles, several variants of β-$Li_{0.5}TiO_2$ could nucleate on different parts of the surface. As these nuclei, having different orientations relative to the original anatase particle, grow inward, they will start impinging, resulting in an increase in elastic strain energy. Overcoming the elastic strain energy for continued growth requires an under potential during discharge, thereby resulting in hysteresis in the voltage vs. lithium composition curve. Stresses arising from the coexistence of several orthorhombic variants within the original anatase particle could also become large enough to cause particle fracture, leading to electrode degradation.

3.4 Conclusion

We have calculated key thermodynamic and kinetic properties of lithiated anatase from first principles, allowing us to shed light on the origins of important limitations of this insertion compound in Li-ion battery applications. Our prediction of a remarkably low Li diffusion coefficient in $LiTiO_2$ and a high solubility limit of ordered $Li_{0.5}TiO_2$ explains the limited capacity of $x = 0.6$. The TiO_2 to $Li_{0.5}TiO_2$ transformation has much in common with martensitic phase transformations, exhibiting strain invariant planes for two-phase coexistence. Furthermore, we predict one-dimensional Li diffusion within ordered $Li_{0.5}TiO_2$ in a direction parallel to the strain invariant planes between anatase TiO_2 and ordered $Li_{0.5}TiO_2$, implying that Li must enter electrode particles at TiO_2 exposed surfaces. This insight provides clear guidance as to how capacity and rates can be maximized and hysteresis minimized during the α to β transformation by controlling particle shape relative to crystallographic directions of anatase.

CHAPTER IV

Coarse Graining Vacancies in Binary Alloys Where the Vacancy Concentration is Very Low

4.1 Introduction

All crystalline solids contain imperfections, the most common of which are vacancy and interstitial point defects. Their thermodynamic origin is often entropic as defect formation energies tend to be positive. While the nature of point defects in single component solids or highly ordered compounds has received much experimental and theoretical attention [55, 56, 57, 58, 59, 60, 61], far less effort has been devoted to understanding the nature and composition dependence of point defects in disordered multi-component solids. Almost all metals used in structural applications are alloys containing a variety of elements that are added to optimize a mix of mechanical, kinetic and phase stability related properties [62, 63]. Alloys of semiconducting compounds are increasingly utilized in electronic applications and are also actively pursued in thermoelectric applications as a way to reduce thermal conductivity [64, 65, 66, 67]. Changing the overall composition of an alloy should affect the equilibrium point defect concentration, as point defects will interact differently with the various components of the solid. Furthermore, the point defect concentration is likely to depend on the degree of short and long-range order, which itself is a function of temperature and overall concentration.

Although the presence of low concentrations of point defects has little effect on the overall thermodynamic properties of a solid and is unlikely to alter the relative stability between different phases, it does play a crucial role in determining electronic and atomic transport properties. Vacancies, interstitials, and more complex antisite or dumbbell-like defects scatter Bloch states thereby resulting in lower electronic conductivity. In semiconductors, they can also alter the Fermi level and thereby

modify the number of free carriers, either by trapping them or donating them to the conduction band.

Point defects are especially important in mediating atomic transport within the crystalline state. Interstitial point defects are typically more mobile [48, 42, 47, 27, 68], but vacancies are essential to redistribute substitutional elements within alloys [69]. The Kirkendall effect is among the most pronounced manifestations of vacancy mediated substitutional diffusion within alloys and arises due to a difference in vacancy exchange frequencies among the various components of the alloy [69, 70, 71, 72]. Any concentration gradient in such alloys results in a net vacancy flux in a direction opposite to the flux of the fastest diffuser. In the presence of vacancy sources and sinks such as dislocations and grain boundaries, a net vacancy flux results in a rigid drift of the crystal frame of reference, often causing deleterious effects within the solid, such as void formation.

Substitutional diffusion coefficients are to first order proportional to the vacancy concentration [69]. Variations in alloy concentration or the degree of short or long-range order will affect the vacancy concentration and thereby the mobility of the constituents of the alloy. There is limited understanding of the dependence of the equilibrium vacancy concentration on alloy concentration and degree of order due to difficulties in directly and precisely measuring vacancy concentrations in multi-component solids. Such understanding is crucial in high temperature applications relying on heterostructures with strong built in chemical potential gradients that drive interdiffusion [72, 73]. It is also of importance in thermoelectric applications where temperature gradients can result in driving forces for demixing, which can be enhanced by high concentrations of point defects.

Here, we develop statistical mechanical methods to predict the thermodynamic properties of vacancies within multi-component solids from first principles. We introduce a coarse graining procedure that enables the prediction of very dilute vacancy concentrations and their associated thermodynamic properties with Monte Carlo simulations. We apply this approach to a study of vacancies in HCP based Ti-Al binary alloys to explore the role of concentration and variations in both short-range and long-range order on the equilibrium vacancy concentration. We find a strong dependence of the equilibrium vacancy concentration on Al concentration and degree of long-range order, especially at low temperature.

4.2 Methods

4.2.1 Alloy Hamiltonian and vacancies

A cluster expansion is a mathematical tool with which to describe any property of a multi-component crystalline solid that depends on how the various components of the solid are arranged within the crystal. It relies on occupation variables assigned to each site within a crystal that can take on discrete values depending on the specie occupying the site. In a binary A-B alloy, spin-like occupation variables, σ_i, are typically used, which take a value of $+1$ if site i in the crystal is occupied by B and -1 if it is occupied by A. Polynomials constructed by taking products of occupation variables belonging to all possible clusters of sites, including clusters containing only one site (a point cluster), pair clusters, triplet clusters, and so forth, can then be shown to form a complete and orthonormal basis in configuration space [22]. Hence, any property of the crystal that depends on how the A and B atoms are arranged on the crystal can be expanded in terms of these polynomial basis functions. The fully relaxed energy of the crystal for example can be written as

$$E\left(\vec{\sigma}\right) = V_0 + \sum_{\alpha} V_\alpha \cdot \Phi_\alpha\left(\vec{\sigma}\right) \tag{4.1}$$

where $\vec{\sigma} = \{\sigma_1, ..., \sigma_i, ..., \sigma_M\}$ denotes the collection of all occupation variables in the crystal, V_0 and V_α are expansion coefficients, to be parameterized with a first-principles total energy method and

$$\Phi_\alpha\left(\vec{\sigma}\right) = \prod_{i \in \alpha} \sigma_i \tag{4.2}$$

are cluster functions defined as the product of occupation variables of sites belonging to a cluster of crystal sites α. The constant term is equal to the average energy of the crystal in the fully disordered state when there are an equal number of A and B atoms. In the fully disordered state at $x = 1/2$, the averages of all the cluster functions are zero since the occupation variables for different sites are uncorrelated and their average value at $x = 1/2$ is zero. The above expression for the configurational energy of the crystal can thus be viewed as an expansion around the fully disordered alloy at $x = 1/2$. This feature is a result of the particular choice of values that the occupation variables σ_i can take. Alternative choices for the values of the occupation variables are possible [74, 75] and may be more convenient for particular applications.

Most metallic alloys and multi-component ceramics of technological importance

have a solvent, which is the dominant specie, and a variety of solutes that have significantly lower concentrations than the solvent. Important examples include alloyed steels, which are Fe rich, and Ni-based super-alloys. Especially the vacancies within a substitutional alloy, which needs to be treated as an explicit component, will have very low concentrations. For these cases, it is more convenient to use an array of occupation variables p_i^B which are 1 if site i is occupied by specie B and zero otherwise. For an n-component solid, $n-1$ such occupation variables must be assigned to each site. These occupation variables are linearly related to the spin like occupation variables σ_i [76]. While there is no restriction on the choice of $n-1$ occupation variables to explicitly work with, it is most convenient to introduce occupation variables for the solutes only. For a binary alloy also containing vacancies, we would then use p_i^B and p_i^{Va} corresponding to the occupation variables for the solute B and the vacancy 'Va'. In terms of these occupation variables, the total energy of the crystal can be written as

$$E\left(\vec{p}\right) = E_0 + \sum_{\alpha} E_{\alpha}^{\vec{D}} \cdot \Lambda_{\alpha}^{\vec{D}}\left(\vec{p}\right) \tag{4.3}$$

where $\vec{p} = \left\{p_1^B, ..., p_i^B, ..., p_M^B, p_1^{Va}, ..., p_i^{Va}, ..., p_M^{Va}\right\}$ is the collection of all occupation variables for each crystallographic site and E_0 and $E_{\alpha}^{\vec{D}}$ are expansion coefficients, again to be determined with a first-principles total energy method. The basis functions are products of occupation variables belonging to sites of a cluster α and can be written as

$$\Lambda_{\alpha}^{\vec{D}}\left(\vec{p}\right) = \prod_{i \in \alpha} p_i^{D(i)} \tag{4.4}$$

In this expression, the index i runs over the sites of a cluster α while $\vec{D} = \{D(i)\}$ labels the type of occupation variable at each site i (i.e. p_i^B or p_i^{Va}). All cluster basis functions that can be mapped onto each other by a space group symmetry operation of the crystal will have the same expansion coefficient $E_{\alpha}^{\vec{D}}$. In contrast to a cluster expansion expressed in terms of spin-like occupation variabes, σ_i, the constant term, E_o, in Equation 4.3, is now the energy of the pure solvent, as then all the occupation variables are equal to zero. The above expression can therefore be viewed as an expansion relative to the energy of the crystal containing only solvent atoms A. Hence, for solvent rich alloys we can expect the above expression to converge more rapidly than an equivalent expansion in terms of spin occupation variables. In this work, we develop a multi-component cluster expansion using occupation variables

p_i^B and p_i^{Va} (as opposed to spin occupation variables) to describe the configurational energy of a multi-component solid containing a dilute concentration of vacancies.

4.2.2 Partition function of a binary alloy containing vacancies

Calculating the equilibrium vacancy concentration in binary alloys when their compositions are very low using a cluster expansion and Monte Carlo simulations requires a very large number of Monte Carlo passes. An equilibrium vacancy concentration of 10^{-12} in a Face Centered Cubic (FCC) based alloy, for example, will require on average 109 Monte Carlo passes in a $10 \times 10 \times 10$ Monte Carlo cell to sample the occurrence of a single vacancy. The statistics using traditional Metropolis Monte Carlo will therefore be poor and will require exorbitant simulation time. Since the occurrence of vacancies at these equilibrium vacancy concentrations is so rare, though, it becomes feasible and sufficiently accurate to perform a coarse graining procedure combined with a low-temperature-like expansion of the partition function. This is described below.

An A-B binary alloy (e.g. Ti-Al) containing vacancies is, strictly speaking, a ternary system. Within lattice Monte Carlo simulations, we work in the grand canonical ensemble with a fixed number of crystal sites M. Thus the numbers of atoms of each component are not independent due to the constraint that $N_A + N_B + N_{Va} = M$. Because A is the solvent, we explicitly track N_B and N_{Va}. The partition function within this grand canonical ensemble when considering only configurational excitations can be written as

$$Z = \sum_{\vec{p}} e^{-\Omega(\vec{p})/kT} \tag{4.5}$$

where

$$\Omega\left(\vec{p}\right) = E\left(\vec{p}\right) - N_B\tilde{\mu}_B - N_{Va}\tilde{\mu}_{Va} \tag{4.6}$$

is the grand canonical energy,

$$\tilde{\mu}_B = \mu_B - \mu_A \tag{4.7}$$

$$\tilde{\mu}_{Va} = \mu_{Va} - \mu_A \tag{4.8}$$

and $E\left(\vec{p}\right)$ is the energy of configuration $\vec{p}$. The generalized chemical potentials are

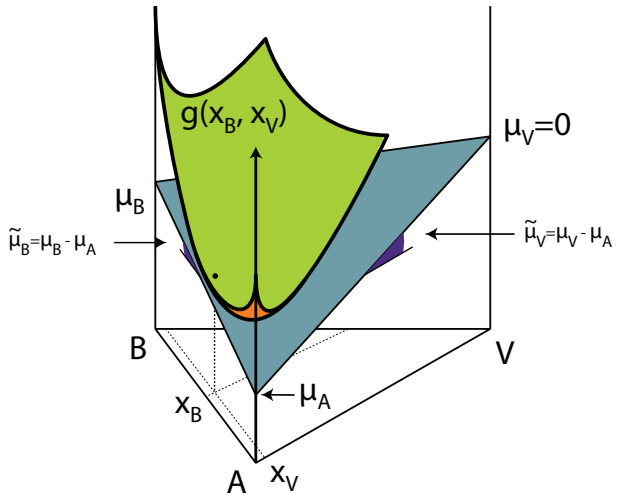

Figure 4.1. Ternary free energy with schematic of chemical potentials and zero vacancy chemical potential.

related to the Gibbs free energy of the solid according to

$$\tilde{\mu}_B = \frac{\partial g}{\partial x_B} \qquad\qquad \tilde{\mu}_{Va} = \frac{\partial g}{\partial x_{Va}} \tag{4.9}$$

where g is the Gibbs free energy per crystal site of the alloy and $x_i = N_i/M$. This can be shown starting from the differential form of the Gibbs free energy $G = Mg$

$$dG = -SdT + VdP + \mu_A dN_A + \mu_B dN_B + \mu_{Va} dN_{Va} \tag{4.10}$$

which with $dN_A = dM - dN_B - dN_{Va}$ becomes

$$dG = -SdT + VdP + (\mu_B - \mu_A)\, dN_B + (\mu_{Va} - \mu_A)\, dN_{Va} + \mu_A dM. \tag{4.11}$$

Within Monte Carlo simulations with periodic boundary conditions, M is constant and therefore $dM = 0$. Then holding T and P constant, we have

$$dG = \tilde{\mu}_B dN_B + \tilde{\mu}_{Va} dN_{Va} \tag{4.12}$$

which, after normalization by M yields the relations between generalized chemical potentials $\tilde{\mu}_i$ and partial derivatives $\partial g/\partial x_i$.

Most alloys of technological interest contain grain boundaries along with a particular density of dislocations that can act as local vacancy sources and sinks. These extended defects can therefore regulate an equilibrium vacancy concentration within the alloy. The vacancy concentration, therefore, cannot be controlled experimentally

and the solid will pick an equilibrium vacancy concentration that minimizes the Gibbs free energy at constant T, P, N_A and N_B. Mathematically this is equivalent to setting the vacancy chemical potential equal to zero

$$\mu_{Va} = \left(\frac{\partial G}{\partial N_{Va}}\right)_{T,P,N_A,N_B} = 0 \tag{4.13}$$

The vacancy chemical potential in a ternary alloy can be written in terms of the Gibbs free energy of the alloy according to

$$\mu_{Va} = g\left(x_B, x_{Va}\right) - x_B \cdot \frac{\partial g}{\partial x_B} + \left(1 - x_{Va}\right) \cdot \frac{\partial g}{\partial x_{Va}} \tag{4.14}$$

which, with the relations between generalized chemical potentials and partial derivatives, can be rewritten as

$$\mu_{Va} = g\left(x_B, x_{Va}\right) - x_B \cdot \tilde{\mu}_B + \left(1 - x_{Va}\right) \cdot \tilde{\mu}_{Va}. \tag{4.15}$$

Setting the vacancy chemical potential equal to zero, we obtain a relationship between $\tilde{\mu}_B$ and $\tilde{\mu}_{Va}$ specifying the path in chemical potential space corresponding to an equilibrium vacancy concentration

$$\tilde{\mu}_{Va} = -\frac{g\left(x_B, x_{Va}\right) - x_B \cdot \tilde{\mu}_B}{\left(1 - x_{Va}\right)}. \tag{4.16}$$

4.2.3 Coarse graining the vacancies in an alloy partition function

Configurations with vacancies have much higher grand canonical energies than configurations without vacancies, and therefore have a much lower probability of occurrence compared to purely binary A-B configurations. Here we develop a coarse graining scheme valid for a grand canonical Monte Carlo simulation of a crystal having periodic boundary conditions. We proceed by writing the sum over all configurations $\vec{p}$ as first a sum over binary configurations $\vec{s}$ followed by a sum over all configurations obtained by inserting vacancies into the binary A-B configuration $\vec{s}$, which we denote by $\vec{q}(\vec{s})$. To avoid double counting of configurations containing vacancies, we only sum over vacancy configurations $\vec{q}(\vec{s})$ obtained from $\vec{s}$ by exchanging either A or B with a vacancy, but not both.

$$Z = \sum_{\vec{s}} \sum_{\vec{q}(\vec{s})} e^{-\Omega(\vec{q}(\vec{s}))/kT} \tag{4.17}$$

$$Z = \sum_{\vec{s}} e^{-\Omega(\vec{s})/kT} \sum_{\vec{q}(\vec{s})} e^{(-\Omega(\vec{q}(\vec{s}))-\Omega(\vec{s}))/kT} \tag{4.18}$$

For fixed binary configuration $\vec{s}$, we can introduce a coarse-grained vacancy free energy:

$$\Delta\Phi_{\text{vac}}\left(\vec{s}\right) = -kT \ln\left(\sum_{\vec{q}(\vec{p})} e^{-\Delta\Omega(\vec{q}(\vec{s}))/kT}\right) \tag{4.19}$$

with

$$\Delta\Omega\left(\vec{q}\left(\vec{s}\right)\right) = \Omega\left(\vec{q}\left(\vec{s}\right)\right) - \Omega\left(\vec{s}\right) \tag{4.20}$$

equal to the cost in the grand canonical energy of introducing vacancies having configuration $\vec{q}(\vec{s})$ in a binary configuration $\vec{s}$ at constant $\tilde{\mu}_B$ and $\tilde{\mu}_{Va}$. With this definition for a coarse grained grand canonical free energy, we can rewrite the full partition function as

$$Z = \sum_{\vec{s}} e^{-(\Omega(\vec{s})+\Delta\Phi_{\text{vac}}(\vec{s}))/kT} \tag{4.21}$$

where the sum extends only over binary configurations, all ternary configurations containing vacancies having been coarse grained out. The coarse-grained vacancy free energy for a particular binary configuration $\vec{s}$ can be written as

$$\Delta\Phi_{\text{vac}}\left(\vec{s}\right) = -kT \ln\left(1 + \sum_{\vec{q}(\vec{s})\neq\vec{s}} e^{-\Delta\Omega(\vec{q}(\vec{s}))/kT}\right) \tag{4.22}$$

If the vacancy formation energies are very high, the sum of exponentials will be very small. Thus, analogously to a low-temperature expansion, we can Taylor expand the

logarithm to yield

$$\Delta\Phi_{\text{vac}}\left(\vec{s}\right) = -kT \sum_{\vec{q}(\vec{s})\neq\vec{s}} e^{-\Delta\Omega(\vec{q}(\vec{s}))/kT} \tag{4.23}$$

For very high vacancy formation energies (i.e. very low vacancy concentrations), the exponentials at moderate temperatures (i.e. temperature corresponding to very low equilibrium vacancy concentrations) will all be small. In a finite sized Monte Carlo cell with periodic boundary conditions, configurations $\vec{q}(\vec{s})$ with two or more vacancies will lead to an increase in energy that is very high with concomitant small exponentials. Hence, in evaluating $\Delta\Phi_{\text{vac}}\left(\vec{s}\right)$ in Monte Carlo, we can restrict ourselves to configurations $\vec{q}(\vec{s})$ with only one vacancy at a time.

4.2.4 Monte Carlo Algorithm

The above coarse-graining procedure effectively reduces a ternary problem to one where only binary configurations need to be explicitly sampled. In Monte Carlo simulations, we therefore need only sample binary configurations. The coarse grained Monte Carlo algorithm then takes the form:

1. Initialize a binary configuration $\vec{s}$.
2. Pick a site in the crystal at random.
3. Consider the replacement of the atom at that site with the other component. We denote this as a change in a binary configuration from $\vec{s}$ to $\vec{s}'$.
4. Calculate the change in coarse grained free energy:

$$\Delta\Theta = \Omega\left(\vec{s}\right) + \Delta\Phi_{\text{vac}}\left(T, \vec{s}'\right) - \Omega\left(\vec{s}\right) - \Delta\Phi_{\text{vac}}\left(T, \vec{s}\right)$$

5. If $\Delta\Theta$ is less than zero, accept the new configuration $\vec{s}'$, else accept it if $e^{-\Delta\Theta/kT} > \xi$, where ξ is a random number between 0 and 1.
6. Return to step 2.

In practice, when the equilibrium vacancy concentrations are very low, it may be possible to neglect $\left(\Delta\Phi_{\text{vac}}\left(\vec{s}'\right) - \Delta\Phi_{\text{vac}}\left(\vec{s}\right)\right)$, such that the sampling of binary configurations would take as much effort computationally as a pure binary system.

4.2.5 Equilibrium Vacancy Composition

The equilibrium number of vacancies is equal to the ensemble average of vacancies given by

$$\bar{N}_{Va} = \frac{1}{Z} \sum_{\vec{p}} N_{Va}\left(\vec{p}\right) \cdot e^{-\Omega(\vec{p})/kT} \tag{4.24}$$

$$\bar{N}_{Va} = \frac{1}{Z} \sum_{\vec{s}} e^{-\Omega(\vec{s})/kT} \left(\sum_{\vec{q}(\vec{s}) \neq \vec{s}} N_{Va}\left(\vec{q}\left(\vec{s}\right)\right) e^{-\Delta\Omega(\vec{q}(\vec{s}))/kT} \right) \tag{4.25}$$

If the vacancy concentration is very low and the size of the crystal in the Monte Carlo cell is not too large, then terms corresponding to configurations with two or more vacancies will contribute negligibly to the second sum. If we neglect all configurations with two or more vacancies, the above sum reduces to

$$\bar{N}_{Va} = \frac{1}{Z} \sum_{\vec{s}} e^{-\Omega(\vec{s})/kT} \left(\sum_{\vec{q}(\vec{s}) \neq \vec{s}} e^{-\Delta\Omega(\vec{q}(\vec{s}))/kT} \right) \tag{4.26}$$

which we can write, using Equation 4.23, as

$$\bar{N}_{Va} = \frac{1}{Z} \sum_{\vec{s}} e^{-\Omega(\vec{s})/kT} \cdot \left(-\frac{\Delta\Phi_{\text{vac}}\left(\vec{s}\right)}{kT} \right) \tag{4.27}$$

This expression can be approximated by taking the average of

$$-\frac{\Delta\Phi_{\text{vac}}\left(\vec{s}\right)}{kT} \tag{4.28}$$

in a binary Monte Carlo simulation. The approximation lies in the fact that Z in Equation 4.27 includes microstates with vacancies, while the binary Monte Carlo simulations do not. The vacancy concentration is then

$$x_{Va} \approx -\frac{1}{MkT} \left\langle \Delta\Phi_{\text{vac}}\left(\vec{p}\right) \right\rangle \tag{4.29}$$

where the average is taken over all binary configurations $\vec{s}$ using the coarse grained partition function.

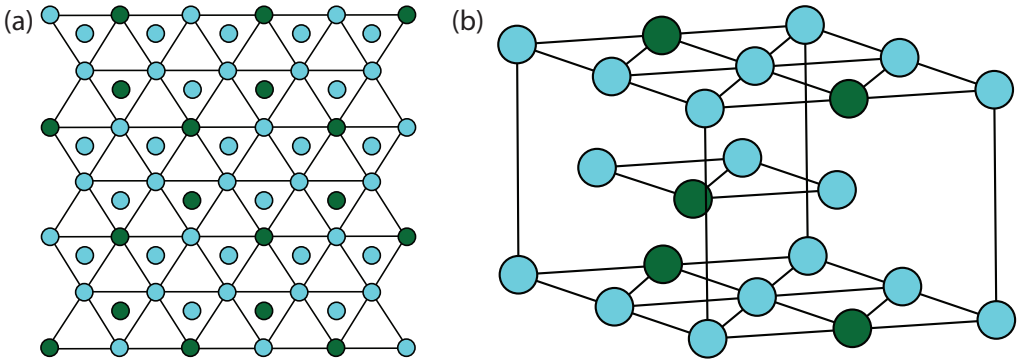

Figure 4.2. Crystal structure schematics of the DO19 (α_2) ordered phase, including (a) a projection view down the c-axis and (b) a 3D representation.

4.3 Results

As an application of this approach, we study the thermodynamics of vacancies in HCP based Ti-Al binary alloys. The HCP form of Ti-Al alloys is thermodynamically stable within the 0-30% Al compositon range. Within this range is a well-known ordered phase, which has a primitive cell that is a $2 \times 2 \times 1$ supercell of the HCP (2 atom) unit cell, with an Al ordering illustrated in Figure 4.2. There is also a large solubility of Al in the HCP Ti-Al solid solution, while the DO_{19} ordered phase is stable over a wide concentration range around perfect stoichiometry of $x = 0.25$. This material will serve as a good model system to explore the effect of alloy concentration and degree of ordering on the equilibrium vacancy concentration.

4.3.1 First-principles parameterization of alloy Hamiltonian

We parameterized a cluster expansion by fitting the coefficients of a truncated form of Equation 4.1 to reproduce the formation energies of different arrangements of Ti, Al, and dilute vacancies over the sites of the HCP crystal structure. The energies of these configurations were calculated with DFT as implemented in the VASP package [18, 21, 20]. We used the PAW pseudopotential method to treat the interaction between valence and core electronic states [21, 20]. A $10 \times 10 \times 5$ k-point mesh, yielding a convergence to within 1.0 meV per atom, was used for the HCP primitive cell and scaled accordingly to achieve equivalent (or greater) k-point densities in the supercells. The atomic positions, lattice parameters, and cell shape were allowed to relax fully using the conjugate gradient approach to minimize the total energy. An energy cutoff of 450 eV was chosen for the plane wave basis set. These calculations were performed without the inclusion of spin polarization. We calculated the energies

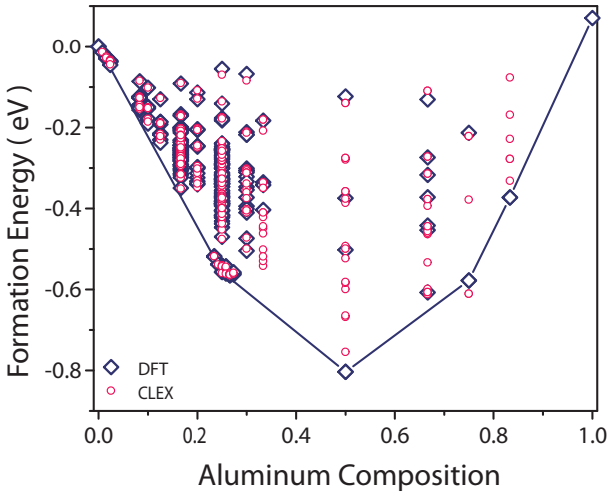

Figure 4.3. DFT (blue diamonds) and cluster expansion predicted (pink circles) formation energies for the Ti-Al binary system as a function of Al composition. Blue lines convex hull and correspond to two-phase regions.

of over 600 binary configurations by enumerating the symmetrically unique orderings of Ti and Al in all distinct supercells containing up to 6 HCP unit cells (up to 12 atoms per cell). In addition to these configurations, we also systematically enumerated dilute perturbations around the ground state configurations, which for the HCP based Ti-Al alloy is pure α-Ti and the ordered α_2-$Ti_3Al(DO_{19})$ phase. These dilute configurational perturbations were enumerated in a 128 atom, $4 \times 4 \times 4$ supercell of the HCP unit cell. For pure Ti in the $4 \times 4 \times 4$ supercell, we calculated the energy of configurations generated by substituting one Ti for an Al, two Ti for a pair of Al and three Ti for a triplet of Al. For the pair and triplet substitutions, we considered all symmetrically distinct Al-Al pairs up to the 8th nearest neighbor and a variety of symmetrically distinct Al-Al-Al triplets of increasing radius. Similar configurations were enumerated in a 128 atom supercell of DO_{19} (i.e. a $2 \times 2 \times 4$ supercell of the DO_{19} unit cell). Within this supercell, we calculated the energies of all anti-site defects (i.e. an Al on the Ti sublattice and a Ti on the Al sublattice), all symmetrically distinct pairs of anti-site defects up to the 8th nearest neighbor and several symmetrically distinct triplets of anti-site defects.

The $4 \times 4 \times 4$ supercells were also used to enumerate different Al arrangements around a single vacancy. The choice of the $4 \times 4 \times 4$ supercell was motivated by a convergence analysis of the vacancy formation energy as a function of supercell size. We calculated the vacancy formation energy using supercells ranging from 42 to 162 atoms. We find that a 128 atom supercell yields a vacancy formation energy to within about 25 meV with respect to the largest 162 atom cell considered. Additionally, we

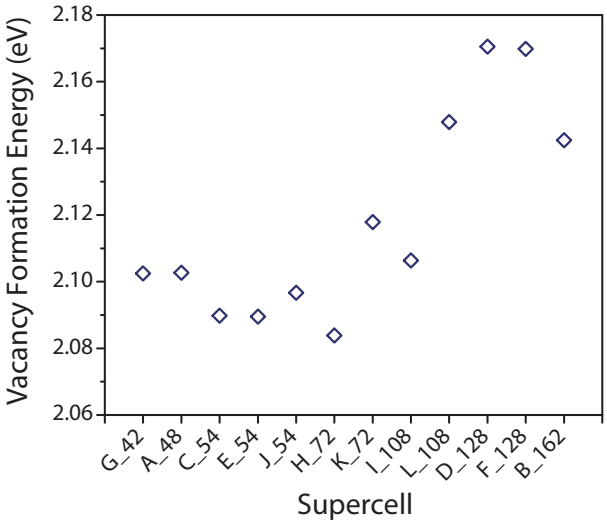

Figure 4.4. Convergence test data for vacancy formation energy in pure HCP-Ti as a function of supercell size and shape.

find that smaller cells are noticeably less suitable as they differ by up to 50 meV from the most accurate value. This is shown in Figure 4.4.

Using the 128 atom 4×4×4 supercell of pure Ti, we calculated the energy of a single vacancy, of symmetrically distinct Al-vacancy pairs up to the 8th nearest neighbor, and of a variety of Al-Al-vacancy triplets. Similar configurations were enumerated in the 128 atom supercell of DO_{19}. A single vacancy was placed on both the Al and Ti sublattices. We also enumerated symmetrically distinct vacancy-anti-site pairs up to the 8th nearest neighbor as well as several symmetrically distinct triplets containing two anti-sites and a vacancy.

A large portion of the more than 600 configurations considered here were found to be mechanically unstable and relaxed to FCC based orderings. This is consistent with the fact that the Ti-Al alloy forms FCC based compounds at aluminum concentrations of $x = 1/2$ and above. We did not include the energies of the mechanically unstable HCP-based ordering when fitting the coefficients of the cluster expansion. We identified configurations that relax to an FCC-based ordering based on the coordination number in the third and fourth nearest neighbor shells. The FCC crystal has 24 and 12 third and fourth nearest neighbors while the HCP crystal has 2 and 18. We only included the energies of configurations that can be mapped onto an HCP parent crystal with certainty, that is, their nearest neighbor tables exactly matched those of the primitive cell with a 0.2 Å tolerance on mapping any given atom into a shell. This leaves only 317 configurations, most of them Ti-rich.

The coefficients of the cluster expansion were determined by fitting to the fully

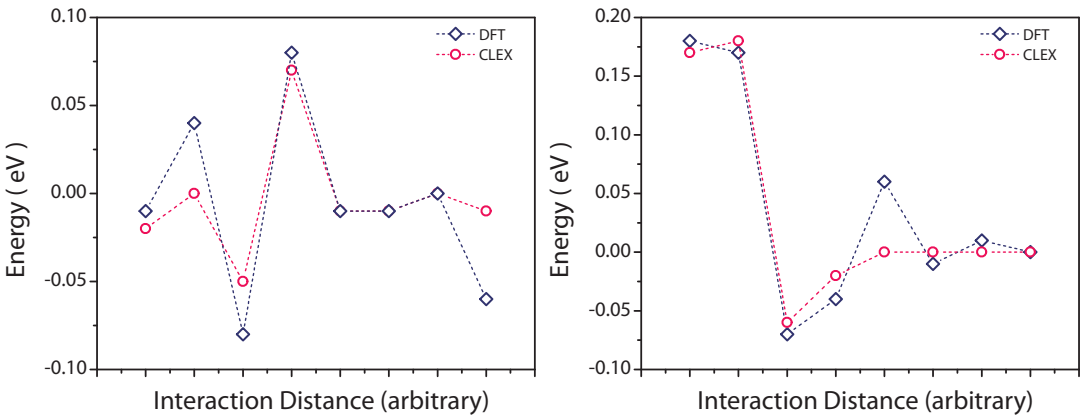

Figure 4.5. Comparison of Al-Va (left) and Al-Al (right) pair cluster relative energies as calculated with DFT (blue diamonds) and predicted with the cluster expansion (pink circles).

relaxed DFT energies of 317 configurations using a genetic algorithm [77] followed by a depth-first-search algorithm to determine the optimal set of non-zero terms in the expansion [24]. We use a number of different metrics to verify the predictive capability of the cluster expansion. The root mean square error between the original DFT energies and the corresponding energies predicted by the cluster expansion is 0.0036 eV per primitive cell (containing two atoms). The leave-one-out CV score is 0.0044 eV per primitive cell. We also ensured that key trends in the first-principles data are reproduced by the cluster expansion. We verified, for example, that the energies of Al-Al and Al-Va pairs within an HCP-Ti crystal have the same qualitative dependence on distance. The DFT calculations predict that the third nearest neighbor Al-Al defect pair in pure Ti is energetically more favorable to form than the first or second nearest neighbor pairs (Figure 4.5), while the energy varies negligibly beyond the third nearest neighbor distance. With Al-Va defects, the energy spikes for the second nearest neighbor, drops for the third, and spikes again for the fourth, but the first nearest neighbor and longer-range pairs have approximately the same energy. These trends are all reproduced with the cluster expansion. Similar trends were reproduced between a pair of anti-site defects and a vacancy-anti-site defect in DO_{19}. As a final test of the quality of the cluster expansion, we sampled representative configurations within grand canonical Monte Carlo simulations at temperatures slightly above the order-disorder transition temperature of DO_{19} and compared their DFT energies with the energies predicted with the cluster expansion. The DFT-PBE energies of eight disordered configurations as sampled in a $4\times4\times4$ supercell of the pimitive cell within Monte Carlo simulations were calculated with VASP. The rms between the DFT

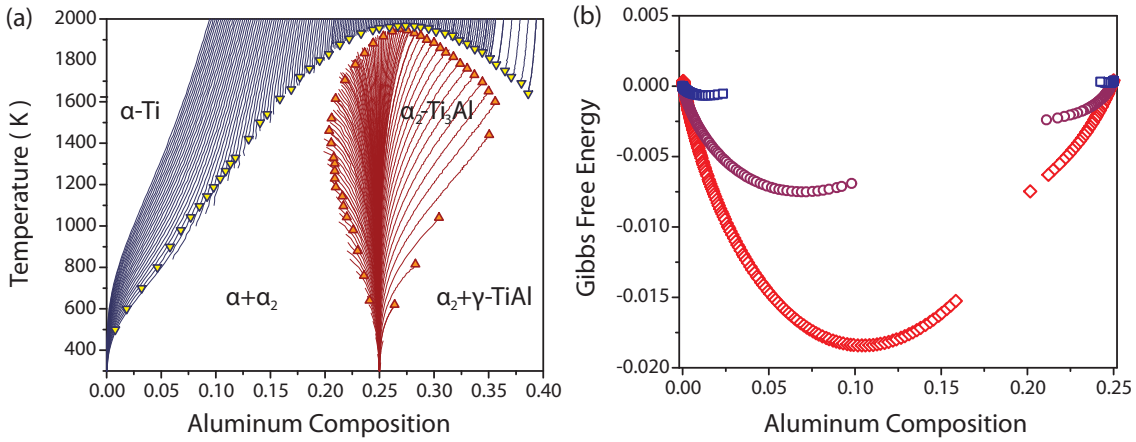

Figure 4.6. (a) Calculated temperature-composition phase diagram for the Ti-Al binary system. Triangles represent points along the predicted phase boundary. Blue (cooling) and maroon (heating) lines are lines of constant chemical potential. (b) Gibbs free energy curves at different temperatures: 600 K (blue squares), 1100 K (purple circles), and 1600 K (red diamonds). These points are obtained using pure α-Ti and α_2-Ti_3Al as references.

energies and those predicted by the cluster expansion for these eight configurations was 0.001 meV per HCP primitive unit cell. This low value, which is of the same order as the numerical accuracy of the direct DFT calculations, indicates that the cluster expansion has a predictive capability with first-principles accuracy.

4.3.2 Monte Carlo Simulations: Phase Equilibrium, Vacancy Composition, and the Effect of Order

The cluster expansion was subjected to grand canonical Monte Carlo simulations to predict a variety of thermodynamic properties, including the temperature-composition phase diagram of HCP based Ti-Al and the equilibrium vacancy concentration as a function of temperature and alloy composition.

The binary temperature-composition phase diagram was constructed by minimizing over Gibbs free energies and grand canonical free energies as obtained with integration techniques of Monte Carlo calculated averages [78, 41, 24]. Figure 4.6 shows the calculated temperature composition phase diagram for Ti-rich HCP Ti-Al. The DO_{19} Ti_3Al ordered phase is predicted to be stable up to 1800 K ($\approx 1500°C$) and is stable over a wide concentration range. A wide two-phase coexistence region separates DO_{19} from a Ti-rich solid solution, while a narrower two-phase region separates DO_{19} from a high Al concentration HCP solid solution. At low temperature, DO_{19} can coexist with an FCC based ordering having TiAl stoichiometry. We did not consider phase stability between the HCP and FCC parent crystal structures. Figure 4.6

shows several Gibbs free energy curves as calculated at different temperatures. The reference states of the free energies shown in Figure 4.6 are pure HCP Ti and the free energy of DO_{19} at $x_{Al} = 0.25$. These free energies were obtained by integrating $\tilde{\mu}_{Al} = \mu_{Al} - \mu_{Ti}$ as a function of alloy concentration x_{Al} according to

$$g\left(x_{Al}\right) = g\left(x_{Al}^{\text{ref}}\right) + \int_{x_{Al}^{\text{ref}}}^{x} \tilde{\mu}_{Al} dx_{Al} \tag{4.30}$$

where $g\left(x_{Al}^{\text{ref}}\right)$ is the Gibbs free energy at a reference concentration x_{Al}^{ref} and the relation between $\tilde{\mu}_{Al}$ and x_{Al} is generated by the grand canonical Monte Carlo simulations. As reference concentration for the free energy of the Ti-rich solid solution, we used $x_{Al}^{\text{ref}} = 0$ where $g\left(x_{Al}^{\text{ref}}\right) = 0$, the formation energy of pure Ti (the configurational entropy is zero at $x_{Al}^{\text{ref}} = 0$). For the free energy of DO_{19}, we used $x_{Al}^{\text{ref}} = 0.25$ and determined the reference Gibbs free energy $g\left(x_{Al}^{\text{ref}}\right)$ by integrating the grand canonical free energy, $\phi = g - \tilde{\mu}_{Al} x_{Al}$, at constant $\tilde{\mu}_{Al}$ as a function of temperature

$$\beta\phi\left(\tilde{\mu}_{Al}, T\right) = \beta_{\text{ref}}\phi\left(\tilde{\mu}_{Al}, T_{\text{ref}}\right) + \int_{\beta_{\text{ref}}}^{\beta} \omega d\beta \tag{4.31}$$

where the grand canonical free energy is defined as $\phi = g - \tilde{\mu}_{Al} x_{Al}$ and $\omega = e - \tilde{\mu}_{Al} x_{Al}$ is the average grand canonical energy calculated with the Monte Carlo simulations. As reference for the above integral, we used the ground state grand canonical energy of DO_{19} at very low temperature (i.e. $\phi\left(\tilde{\mu}_{Al}, T_{\text{ref}}\right) = \omega_{DO_{19}}$).

The Gibbs free energy data, in addition to being essential input for the calculation of the equilibrium phase diagram are also needed to determine the values of $\tilde{\mu}_{Va}$ corresponding to an equilibrium vacancy concentration (i.e. $\mu_{Va} = 0$) according to Equation 4.16. Since the vacancy concentration in the Ti-Al alloy is exceedingly low ($\approx 10^{-17} - 10^{6}$), we can neglect x_{Va} in Equation 4.16 and use the Gibbs free energy of the binary alloy in the absence of vacancies. Figure 4.7 shows all of the data that serve as input parameters for the coarse grained Monte Carlo simulation. The Gibbs free energy in Figure 4.7(b) is the same as that in Figure 4.6(b), but instead of the reference states being pure α-Ti and α_2-Ti_3Al, they are now pure α-Ti and pure FCC-Al. These curves are obtained by integrating (as per Equation 4.30) the chemical potential data in Figure 4.7(a), which is obtained from binary Ti-Al grand canonical Monte Carlo simulations. The points in Figures 4.7(c) and (d) are acquired via Equation 4.16.

We calculated the equilibrium vacancy concentration within grand canonical Monte Carlo simulations by explicitly sampling microstates in the full Ti-Al-Va ternary and

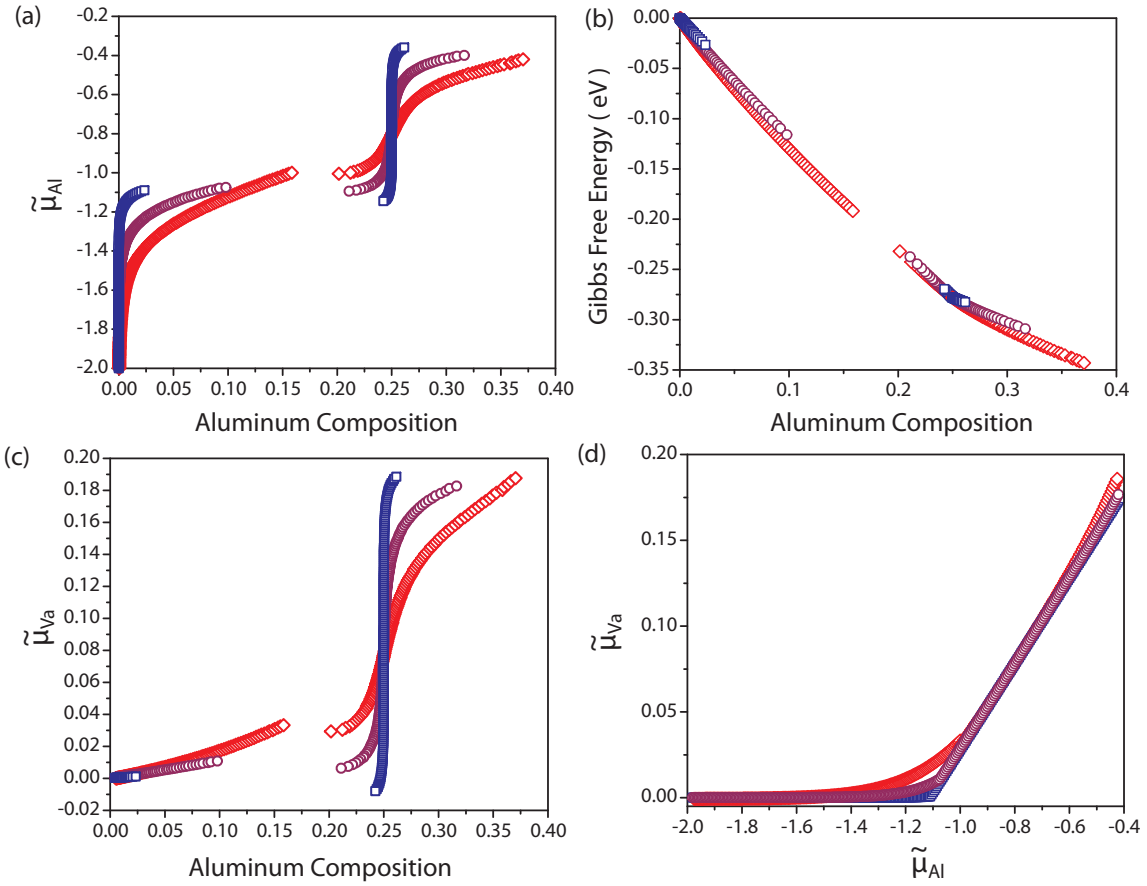

Figure 4.7. Data required as inputs for the coarse grained Monte Carlo simulations: (a) Al chemical potential $\tilde{\mu}_{Al}$ as a function of alloy composition, (b) Gibbs free energy, (c) $\tilde{\mu}_{Va}$ as a function of alloy composition, (d) $\tilde{\mu}_{Va}$ as a function of $\tilde{\mu}_{Al}$.

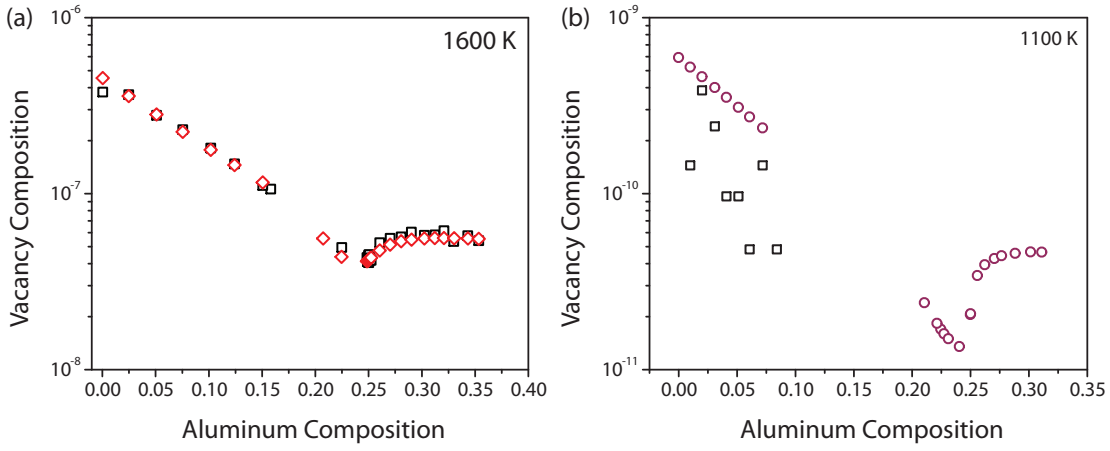

Figure 4.8. Comparison of results obtained with full ternary Monte Carlo simulations (black squares) and the Coarse Grained Monte Carlo method at (a) 1600 K (red diamonds) and (b) 1100 K (purple circles).

by using the coarse-grained binary Monte Carlo algorithm introduced in Section 4.2.4. Figure 4.8 compares the equilibrium vacancy concentrations at 1600 K and 1100 K as calculated with both approaches. The agreement between the full ternary Monte Carlo simulations and the coarse grained binary Monte Carlo simulations seen in Figure 4.8(a) is excellent. In the full ternary simulations, 6 to 12 million Monte Carlo passes were required (a Monte Carlo pass is the number of attempted site occupant exchanges per site) to attain well-averaged vacancy concentrations. The coarse grained binary Monte Carlo required only on the order of several thousand Monte Carlo passes to achieve the same quality in the average vacancy concentration. We can also see how quickly the ternary approach becomes intractable. Even after 6 million Monte Carlo passes at 1100 K, the data in Figure 4.8(b) is very scattered, and no vacancy events occur in the simulation at all at compositions beyond $x_{Al} = 0.1$. Figure 4.9 shows calculated equilibrium vacancy concentrations at several temperatures. Only the coarse-grained binary Monte Carlo algorithm was viable at the lower temperatures.

The equilibrium vacancy concentration has a strong dependence on the alloy concentration, especially at lower temperatures. At 600 K, for example, the vacancy concentration decreases by three orders of magnitude between the solubility limit of the solid solution and DO_{19} at $x_{Al} = 0.23$. Within DO_{19}, the equilbrium vacancy concentration jumps very rapidly by about two orders of magnitude as the Al concentration increases. The equilibrium vacancy concentration is affected by the availability of energetically favorable local environments. This is determined by the equilibrium degree of short and long-range order between Al and Ti. Figure 4.10 (a) and (b) illustrates the positions of successive nearest neighbor atoms radiating out of a fixed point (in Figure 4.10(a), that point is occupied by a vacancy, and in Figure 4.10(b), it is occupied by an Al anti-site defect). The sizes of the balls correspond to the relative amount of energy that it costs to form a pair defect by placing an Al atom at each of those sites. Figures 4.10(c) and (d) show the average Al concentrations within successive neighboring shells surrounding a vacancy and Al atom, respectively, as a function of alloy concentration, calculated at 1600 K.

If the alloy is completely random, all shell concentrations will equal the Al concentration of the alloy. Deviations from x_{Al} indicate short-range order in the solid solution and long-range order in DO_{19}. As is clear in Figure 4.10, there is some degree of short-range order, even at temperatures as high as 1600 K.

Figure 4.10 gives us some insight into the type of short range ordering we might observe around an Al atom and a vacancy. Each dashed line in Figures 4.10(c) and

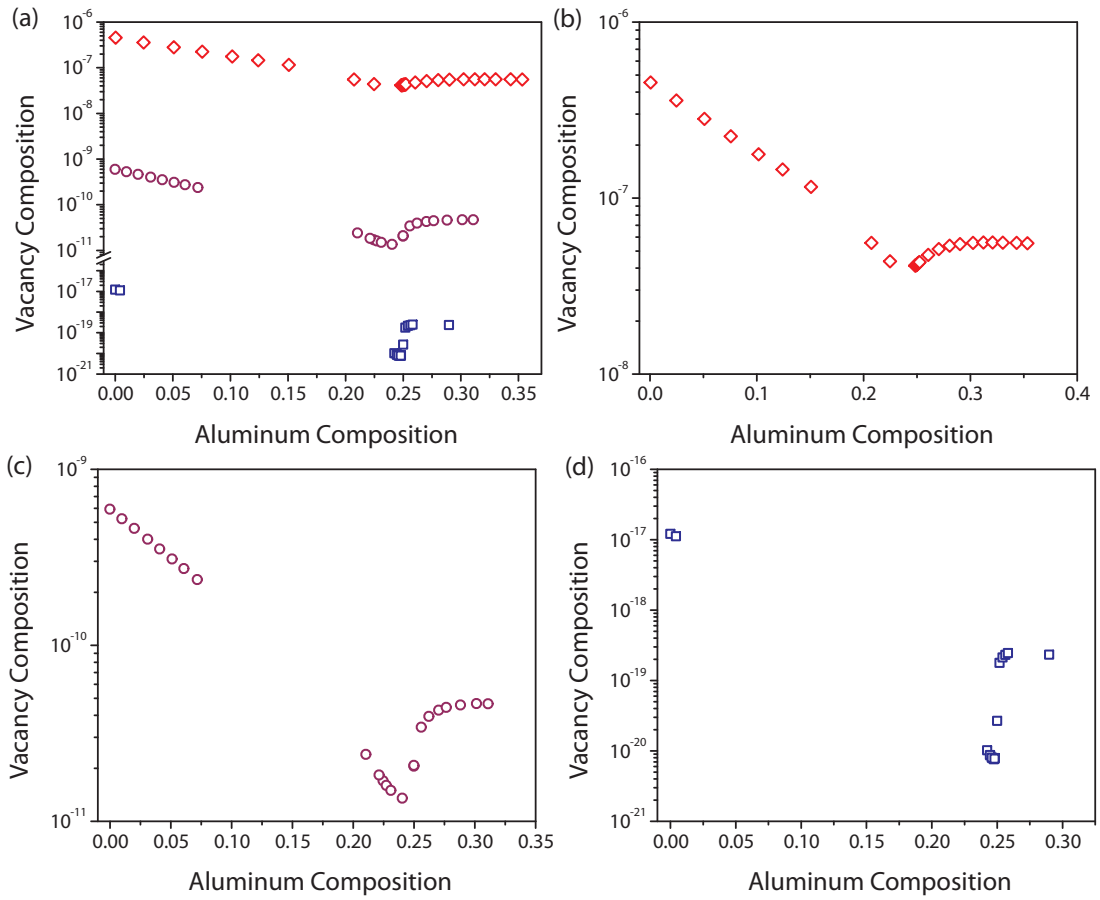

Figure 4.9. Equilibrium vacancy composition data calculated using the coarse grained Monte Carlo method for three different temperatures: 1600 K (red diamonds), 1100 K (purple circles), and 600 K (blue squares).

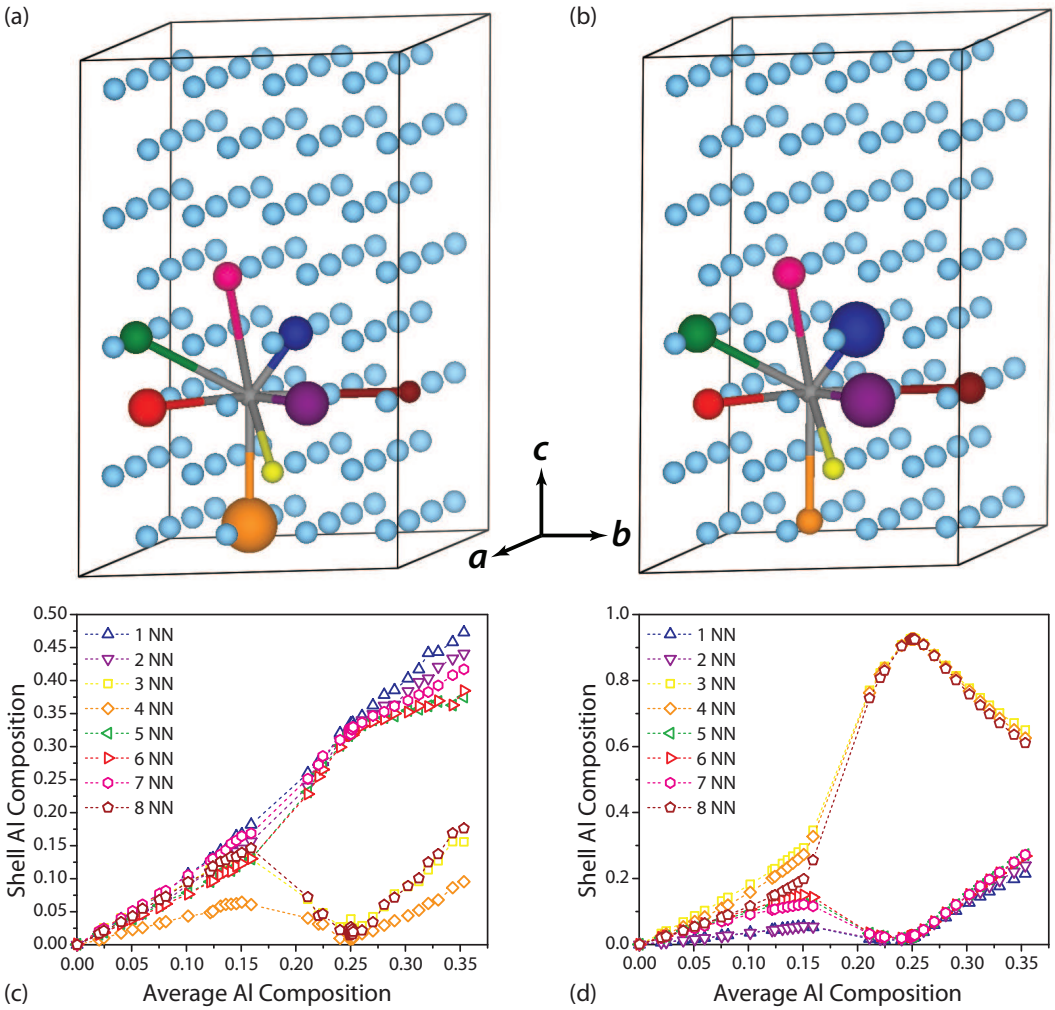

Figure 4.10. Defect formation energetics and Al composition in successive nearest neighbor shells around (a) a vacancy and (b) an Al anti-site defect. The sizes of the balls indicate the relative energy cost of forming the pair defect. In (c) and (d) the Al shell composition is plotted as a function of average Al composition for the vacancy and Al anti-site defects, respectively.The colors consistently correspond to a specific nearest neighbor shell, e.g. the orange ball in (a) and (b) is the fourth nearest neighbor, and the orange line in (c) and (d) is for the fourth nearest neighbor shell.

(d) corresponds to a subsequent nearest neighbor shell around either a vacancy or Al atom, respectively, and we are plotting the Al composition in that shell as a function of average Al composition in the crystal. At $x = 0$, all of the shell composition are zero because no Al atoms are present in pure α-Ti. At $x = 0.25$, however, in the DO_{19} ordered phase, the shell composition gives us the preferred site occupancy. Unsurprisingly, the Al atoms occupy the 3rd, 4th, and 8th nearest neighbor shells, which his consistent with the Al ordering in this phase. We also see some degree of short-range order around vacancies, with a clear tendency for vacancies to prefer local environments in which the fourth nearest neighbor has a lower than average Al concentration. In DO_{19}, the average Al concentrations of neighboring shells around the vacancies indicate that the vacancy prefers the Ti sublattice to the Al sublattice. This is consistent with a zero Kelvin grand canonical free energies, which are most negative for vacancies on the Ti sublattice. Additionally, whenever the shell composition is not equal to the average composition in the two-phase region, we can imagine that some energetics is affecting the atom arrangements. In the Al-Al interaction case, the Al atoms prefer to not be near each other, so the nearest neighbor Al-Al pair defects are particularly costly to form, and this is again confirmed by their nearest neighbor lines deviating from the others. Similarly, the 4th nearest neighbor line that deviates from the average for the Al-Va pairs corresponds to an Al atom occupying the a site in the layer directly below a vacancy, which also appears to be energetically unfavorable.

4.4 Discussion

We have explored the role of composition and variations in the degree of short and long-range order on the equilibrium vacancy concentration in multi-component crystalline solids, using the binary HCP based Ti-Al alloy as an example. A multi-component solid at finite temperature can exhibit a range of short and long-range order. The HCP based Ti-Al alloy exhibits both a solid solution and a stable ordered phase at $x = 0.25$ with a substantial tolerance to deviations from this ideal stoichiometric composition. Variations in temperature and composition in this alloy therefore result in different degrees of short and long-range order. The equilibrium vacancy concentration will depend on the degree of order since the various components of the solid generally interact differently with vacancies, and vacancies have a tendency to prefer particular local environments over others.

Explicitly accounting for vacancies in a two-component solid turns it into a ternary

problem. Here we have used a ternary cluster expansion expressed in terms of polynomials of occupation variables to describe the interactions among Al and between Al and vacancies in an otherwise Ti-rich HCP crystal. The equilibrium vacancy concentration is determined by setting the vacancy chemical potential equal to zero, which is equivalent to minimizing the free energy of the solid with respect to the number of vacancies, holding the number of other components of the solid constant. Because vacancies usually have very low equilibrium concentrations, direct sampling using ternary grand canonical Monte Carlo simulations becomes intractable, especially at low temperature. Exploiting the exceedingly low equilibrium vacancy concentrations of most solids, we have developed a Monte Carlo algorithm that does not explicitly sample vacancy microstates. This is achieved by integrating out all dilute vacancy configurations within a disordered binary solid to obtain a coarse-grained vacancy free energy for each explicitly sampled binary configuration. A comparison between predictions of the full ternary grand canonical Monte Carlo simulations and the coarse-grained binary Monte Carlo at high temperatures demonstrates the validity of the approximations inherent to the coarse graining procedure. The approximations within the coarse grained algorithm become more accurate with decreasing temperature, where the errors incurred by neglecting microstates involving more than one vacancy at a time in a Monte Carlo sized cell become negligible. This new algorithm has allowed us to calculate equilibrium vacancy concentrations at low temperatures with a reasonable number of Monte Carlo passes.

To ensure that the equilibrium short-range order sampled in Monte Carlo simulations is representative of that predicted by density functional theory, we fit the ternary cluster expansion to a large (> 300) database of DFT energies of Ti-Al-vacancy orderings on HCP. Among the configurations used to parameterize the cluster expansion were symmetrically distinct arrangements of a large number of point, pair, and triplet Al and vacancy arrangements within a large supercell of pure Ti and within a supercell of DO_{19} Ti_3Al. We ensured that the cluster expansion accurately reproduces the trends in Al-Al and Al-vacancy pair energies in pure Ti as well as anti-site-anti-site and anti-site-vacancy pair energies in DO_{19}. A comparison with representative high temperature configurations sampled at high temperature with Monte Carlo simulations also demonstrated that the cluster expansion has a predictive capability that matches the numerical accuracy of direct DFT calculations.

The cluster expansion therefore appears to be very accurate in extrapolating DFT energies, including those not used in the fit. The calculated phase diagram using this cluster expansion is similar to previous predictions of the $\alpha + \alpha_2$ phase bounds and

predicts a transition temperature around 1900 K (about 1650°C), a value that is close to, but slightly below, that predicted by van de Walle and Asta [23].

The experimental order-disorder transformation temperature is unknown due to the transformation of HCP Ti-Al to Body Centered Cubic (BCC) Ti-Al at temperatures where DO_{19} Ti_3Al is still stable [7]. While early assessments of the Ti-Al binary phase diagram depicted an order-disorder transition temperature below the transformation of HCP Ti-Al to bcc Ti-Al [6, 79, 80], more recent assessments have concluded that it occurs at temperatures above the HCP to bcc transformation [7, 81]. The predicted order-disorder transition temperature of approximately 1650°C corresponds to the incoherent transformation temperature. It is experimentally very challenging to determine this incoherent transition temperature. Most samples consist of a coherent two-phase mixture of an HCP Ti-rich solid solution, α, and DO_{19} Ti_3Al, α_2 [81, 82]. Coherency strains introduce a free energy penalty that depresses transition temperatures and decreases the widths of two-phase bounds [82, 83, 84]. An additional complexity arises from the fact that HCP Ti is capable of dissolving very high concentrations of oxygen in its interstitial octahedral sites, reaching concentrations as high as $TiO_{1/2}$. Many of the HCP based Ti-Al alloys also contain non-negligible oxygen concentrations, which will have an important effect on the order-disorder transition temperature of DO_{19}. Only a limited number of studies have explored the role of oxygen in modifying the equilibrium phase bounds between α and α_2 [85]. Furthermore, there is a likelihood that dissolved oxygen can couple with coherency strains, for example by relieving a portion of the coherency strain energy penalty of two-phase coexistence by redistributing between the two phases [82]. This further complicates a comparison of the calculated incoherent order-disorder transition temperature to experiment.

Our present study only accounts for configurational degrees of freedom and neglects vibrational excitations. Van de Walle [86] recently incorporated the effect of vibrations in calculating the Ti-rich HCP Ti-Al phase diagram using length transferable force constants (LDTFCs) and a cluster expansion for the coarse-grained vibrational free energies. This study showed that the inclusion of vibrational excitations substantially decreases the DO_{19} order-disorder transition temperature. In fact, within the LDTFC approximation, the inclusion of vibrations decreases the transition temperature to values that are even below the earliest experimental estimates of this temperature. As with the phase diagram, the role of vibrational excitations is also likely to be important in determining the equilibrium vacancy concentration. The same cluster expansion approach as well as the coarse-grained Monte Carlo algorithm

used here can be applied when accounting for vibrational excitations in addition to configurational degrees of freedom.

Our study here has shown that the equilibrium vacancy concentration can vary by several orders of magnitude over relatively small intervals of alloy concentration. In the absence of long-range order, the vacancy concentration is predicted to decrease with increasing Al concentration. In DO_{19} Ti_3Al, the vacancy prefers to occupy the Ti sublattice rather than the Al sublattice. This result is in qualitative agreement with predictions made with embedded atom interatomic potentials as implemented in a mean field framework[87]. A vacancy preference for the Ti sublattice of Ti_3Al causes the vacancy concentration to increase abruptly once the Al concentration increases above the stoichiometric value of $x = 0.25$. An increase in the Al concentration above a stoichiometric Ti_3Al can be achieved in two ways: (i) by adding energetically costly Al anti-sites to the Ti sublattice and (ii) by adding more, albeit also energetically costly, vacancies to the Ti sublattice. The increase in vacancy concentration with Al concentration in α_2 between $x = 0.22$ and $x = 0.35$ agrees qualitatively with the dependence of an effective vacancy formation energy with Al concentration as determined with positron lifetime measurements [88] and with embedded atom interatomic potentials [87].

An accurate description of vacancy solute interactions is a crucial input for predictions of diffusion coefficients in multi-component solids [89, 90]. Interdiffusion coefficients are to first order proportional to the vacancy concentration [69]. The interdiffusion coefficient will therefore be very sensitive to large variations in the equilibrium vacancy concentration as a function of alloy concentration. The preference of vacancies for the Ti sublattice of DO_{19} Ti_3Al [91] will have important consequences for diffusion in the ordered phase [87]. The Ti sublattice forms an interconnected network, connected by nearest neighbor pairs. Hence, vacancies on the Ti sublattice can freely diffuse through DO_{19} without introducing any more disorder. The correlation factor for vacancies will therefore be quite high. In contrast, when vacancies prefer the minority sublattice (such as the Al sublattice in DO_{19} or the Li sublattice of $L1_2$ Al_3Li), which do not form an interconnected network, they will generally be trapped as typical nearest neighbor vacancy-atom exchanges result in an increase in disorder. The vacancy correlation factor is then very low [89]. The results here in combination with a prediction of the relevant diffusion coefficients [69] are of value in Allen-Cahn and Cahn-Hilliard type approaches to study precipitation of DO_{19} in supersaturated HCP based Ti-Al solid solutions.

4.5 Conclusion

We have implemented the cluster expansion formalism to calculate a first principles phase diagram for the HCP based Ti-Al binary alloy in the 0-30% Al composition range. The resulting effective Hamiltonian is incorporated in a new coarse grained Monte Carlo method, which is described in detail, for the study of equilibrium vacancy composition and relevant thermodynamic properties in multi-component systems with dilute vacancies. In the HCP based Ti-Al sytem, we find a strong dependence of the equilibrium vacancy composition on Al composition and degree of long range order, especially at low temperature.

CHAPTER V

Outlook

The 21st century is truly the age of information. Every day computers become more powerful and efficient, scientists become more innovative, and the fields of research that perhaps seemed disparate just a few decades ago become more and more intimately intertwined. In this realm, developing cutting edge computational methods that take advantage of new technologies while working in close proximity with experimentalists to reach an ever deeper and more complete understanding of the world around us is the key to driving innovation. Well developed computational models can not only describe a phenomenon that has already been observed, but also predict the behavior of materials that cannot be measured or propose novel materials systems that do not yet exist.

The work described in this dissertation looks closely at two rather different systems – oxides for lithium-ion battery electrodes and titanium-aluminum structural alloys. While their potential real world applications are quite dissimilar (rechargeable batteries and airplane engines, respectively), we are able to incorporate our in-house computational modeling suite very effectively in both cases to draw conclusions that can be useful for future studies of those systems and the efforts to implement these materials in industrial applications. We have shown here that incredible insight can be gained from studying a system's behavior as a function of configurational disorder and that these results can be acquired relatively inexpensively using cluster expansion and Monte Carlo techniques.

We have elucidated the peculiar behavior of anatase TiO_2 as a function of increased lithium composition, identifying an ordered phase at $x = 0.5$ and showing that diffusion in this phase is purely one-dimensional. We explained why this material can only be lithiated fully at the nanoscale and suggest some potential preferred particle shapes to maximize the actual lithiation of anatase electrodes.

For the Ti-Al system, we developed a new coarse grained Monte Carlo method that allows for the rapid and accurate calculation of the equilibrium vacancy composition as a function of alloy composition in any alloy system with dilute vacancies. These results are essential for the study of diffusion and microstructure evolution in structural alloys (and potentially many other materials). The data we have generated with our approach is also integral as input for further modeling efforts by our collaborators, specifically phase field modeling to study precipitate evolution. Lastly, of course, we hope to continue the back-and-forth relationships with experimental groups with whom we continually attempt to reconcile results to gain new insights into the physics that drives our universe.

As technology continues to advance, new methods will emerge, and old methods will be refined for accuracy and to accommodate higher and higher degrees of complexity. Alongside them, experimental equipment will evolve also, and engineers designing new materials, devices, and ideas will continue to push the frontiers of science. I, for one, am honored to have had the opportunity to make my contribution.

APPENDICES

APPENDIX A

Group Theory and Crystal Symmetry

A.1 Group Theory and Crystal Symmetry

A.1.1 Introduction

A group consists of a set of elements and an operation that combines any two of those elements to obtain a third element. Symmetry groups specifically consist of a set of transformations (e.g. rotations, reflections) that leave a particular object unchanged and the operation of subsequently applying these transformations. Mathematical groups must abide by the four group axioms: closure, associativity, identity, invertibility.

Closure: For all $a, b \in G$, $(a \cdot b) \in G$. In other words, the operation obtained by combining any two operations in G and applying them in rapid succession is also an operation in G.
Associativity: For all a, b, and $c \in G$, $(a \cdot b) \cdot c = a \cdot (b \cdot c)$, i.e. the way in which the operations are grouped does not change the result (as long as the order in which they appear is preserved).
Identity: There exists an element $e \in G$ such that $e \cdot a = a \cdot e = a$ holds for every element in G. The identity element is unique.
Invertibility: For every element $a \in G$, there exists an element $b \in G$, such that $a \cdot b = b \cdot a = e$ or $aa^{-1} = a^{-1}a = e$, i.e. the inverse of every element of the group is also contained in the group and is unique.

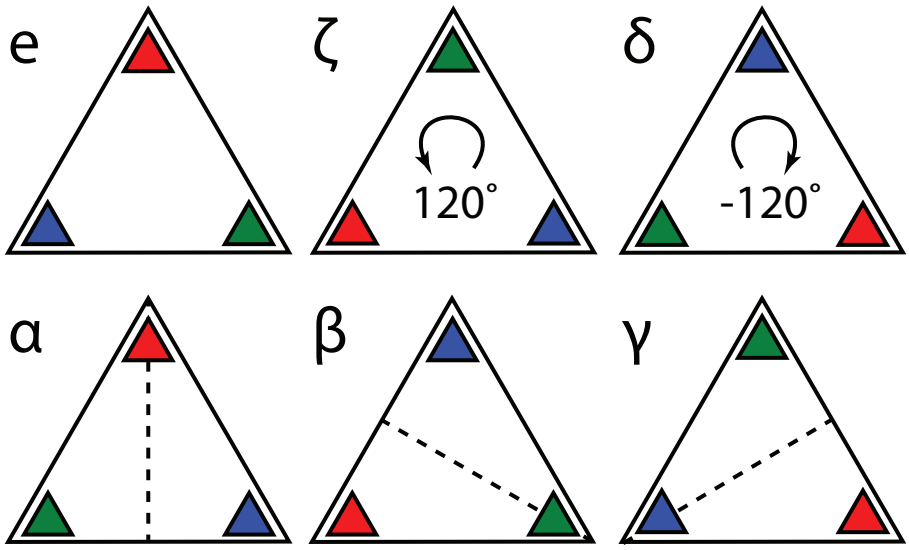

Figure A.1. Shown are the 6 symmetry operations in the group C_{3v}, which map an equilateral triangle onto itself.

It is worth noting that for any two elements a and b of a group, the relation $a \cdot b = b \cdot a$ does not necessarily hold, i.e. they may, but are not required to commute. If all elements of a group commute, then it is a cyclic or Abelian group. Abelian groups have a number of other unique properties including, for example, that all of their elements are self-conjugate and that they have a single generating element. The order of a group is equal to the number of elements it contains.

A.1.2 A Simple Example: The Symmetry of an Equilateral Triangle

An example commonly used to teach group theory, especially as it relates to crystal symmetry, is that of the symmetry operations on an equilateral triangle, which are shown in Figure A.1.

The first triangle, labeled e, corresponds to the identity element, which leaves the figure unchanged. Then there are two rotations by $\pm 120°(2\pi/3)$, ζ and δ, about an axis coming out of the page and three refections, α, β, γ, through mirror planes with plane normal vectors bisecting the three corners of the triangle for a total of six symmetry operations. Each triangle in Figure A.1 shows how the colored corners are permuted after the application of the corresponding operation. We can convince ourselves that this is, in fact, a group by simply applying different operations one after the other and noticing that the result is equivalent to having applied some (other) operation just once. Additionally, we can determine all of the inverses by looking for an operation that undoes the effect of another operation, e.g. ζ is the inverse of δ

and each mirror place is its own inverse.

There is a number of clever ways to organize and partition groups, and we will start by constructing a multiplication table. A multiplication table, sometimes referred to as a Cayley table, is a tool for describing the structure of a finite group by showing which element results from the combination of any two other elements. Usually, the intersection of row X and column Y is XY, rather than YX, and because non-Abelian groups are not required to commute, the XY entry is not, in general, the same as the YX entry. Thus, the Cayley table for the triangle group can be built as shown in Table A.1 to obtain the final result in Table A.2.

	e	α	β	γ	δ	ζ
e	ee	$e\alpha$	$e\beta$	$e\gamma$	$e\delta$	$e\zeta$
α	αe	$\alpha\alpha$	$\alpha\beta$	$\alpha\gamma$	$\alpha\delta$	$\alpha\zeta$
β	βe	$\beta\alpha$	$\beta\beta$	$\beta\gamma$	$\beta\delta$	$\beta\zeta$
γ	γe	$\gamma\alpha$	$\gamma\beta$	$\gamma\gamma$	$\gamma\delta$	$\gamma\zeta$
δ	δe	$\delta\alpha$	$\delta\beta$	$\delta\gamma$	$\delta\delta$	$\delta\zeta$
ζ	ζe	$\zeta\alpha$	$\zeta\beta$	$\zeta\gamma$	$\zeta\delta$	$\zeta\zeta$

Table A.1. Obtaining the elements of the multiplication table for equilateral triangle symmetry group C_{3v}.

	e	α	β	γ	δ	ζ
e	e	α	β	γ	δ	ζ
α	α	e	ζ	δ	γ	β
β	β	δ	e	ζ	α	γ
γ	γ	ζ	δ	e	β	α
δ	δ	β	γ	α	ζ	e
ζ	ζ	γ	α	β	e	δ

Table A.2. Complete multiplication or Cayley table for equilateral triangle symmetry group C_{3v}.

Note that usually the identity element appears first in the Cayley table, which allows for the omission of the separate row and column headers. One useful property of the multiplication table is that each group element may only appear exactly once in every row and every column. Often, this rule alone can allow us to fill in an incomplete multiplication table without any prior knowledge of its actual elements. It is also worth mentioning that the Cayley tables of Abelian groups always have only identity elements on the diagonal; thus, we can infer from this multiplication table that C_{3v} is not a cyclic group.

A.1.3 Conjugacy Classes

Crystal symmetry groups, like all mathematical groups, can be partitioned into conjugacy classes. Given a group G, two elements of G, a and b are conjugate to each other if there exists an element in G such that

$$SaS^{-1} = b.$$

In other words, a and b are similar matrices, and S is the similarity transformation. Thus, all similarity transformations between a and b belong to a single conjugacy class and share the same rank, determinant, trace, and eigenvalues (though not necessarily the eigenvectors). Note that because these are equivalence classes, each class groups together elements that represent a particular type of symmetry, e.g. 90° rotations about equivalent axes. Each group element belongs to exactly one conjugacy class, and the identity element is always in a class by itself. If G is an Abelian group, then every class contains exactly one element because the elements of cyclic groups are self-conjugate. Note also that while conjugacy classes are sets, they are not groups themselves because they do not have identity elements (with the exception of the identity class, which is a trivial group). The equilateral triangle group we introduced previously has three conjugacy classes that we can think of as the identity class (containing e), the rotation class (containing δ and ζ), and the reflection class (containing α, β, and γ).

A.1.4 Subgroups

A subgroup H is a set of elements within a group G that themselves also form a group. The identity element e by itself is the trivial subgroup of any group, and all other subgroups of G must share the identity element of G, i.e. $e_H = e_G$. If H is a subgroup of G, it is often denoted $H \leq G$, and G is referred to as the overgroup of H. The order of a subgroup must be a divisor of the order of the overgroup.

Exploring the subgroups of a symmetry group can give a great deal of insight into that group's structure and related properties. In crystallography in particular, among the 14 Bravais lattices, there are exactly 32 crystal lattice point groups, but all of these groups are actually subgroups of either the hexagonal close packed (HCP) or face centered cubic (FCC) lattice groups D_{6h} and O_h, respectively. This means, in essence, that we can obtain all of the other crystal lattice groups by strategically removing elements from D_{6h} and O_h.

Another neat property of the multiplication table allows us to quickly find all of

the smallest subgroups of any group. Due to the fact that all of the identity (e) entries that lie on the diagonal of the Cayley table correspond to elements that are their own inverses, they also comprise a subgroup containing only e and the element in that row's (or column's) header. Using Table A.2 for C_{3v}, we find four such small subgroups: the trivial group $\{e\}$ and groups $\{e, \alpha\}, \{e, \beta\}, \{e, \gamma\}$, which are actually all equivalent. For the two diagonal entries in Table A.2 that are not identity, we can "complete the cycle" to find the smallest subgroup containing the elements in those rows/columns. This means that we keep multiplying the result with the starting element (the row header we started with) until we get identity back and add every intermediate element to the subgroup. Thus, because $\delta\delta = \zeta$ and $\delta\zeta = \zeta\delta = e$, we end up with the subgroup $\{e, \delta, \zeta\}$, which makes sense because we already know that δ and ζ are inverses of each other. All of the subgroups we have found so far have order 2 or 3, which are both divisors of 6, the order of G. From here, all other subgroups of G can be found by combining the smallest subgroups with each other and enforcing the group axioms. The group C_{3v} has only 3 distinct subgroups: C_3, C_1, and S_1. The crystal groups are shown in Figure A.2 with all of their subgroup/overgroup relationships.

The centralizer C of a subset L of a group G is a special subgroup of G that contains the elements of G that commute with each element in L. Similarly, the normalizer N of a subset L of a group G contains the elements of G that commute with L as a whole. This difference is subtle, but it lies in the fact that the normalizer condition is less strict. For example, if an element g is in the centralizer of L and element s is in L, then it must be the case that $gs = sg$. However, if g is in the normalizer of L, then it can be the case that $gs = tg$ for some element t as long as t is also in L. The centralizer of the identity class is the entire group. The other two centralizer groups of C_{3v} are: $\{e, \alpha\}$, and $\{e, \delta, \zeta\}$.

A.2 Representation Theory

Representation theory is a field of mathematics that concerns itself with describing abstract algebraic objects with matrices and any operations that may act on those objects in terms of matrix addition and multiplication. This allows us to work with abstract concepts such as group theory in the linear algebra vector spaces that are much more familiar. Thus, in the context of crystal symmetry, a representation will refer to a set of matrices (the symmetry operations), each of which corresponds to a geometrical manipulation of the crystal. Because we work with matrices so frequently,

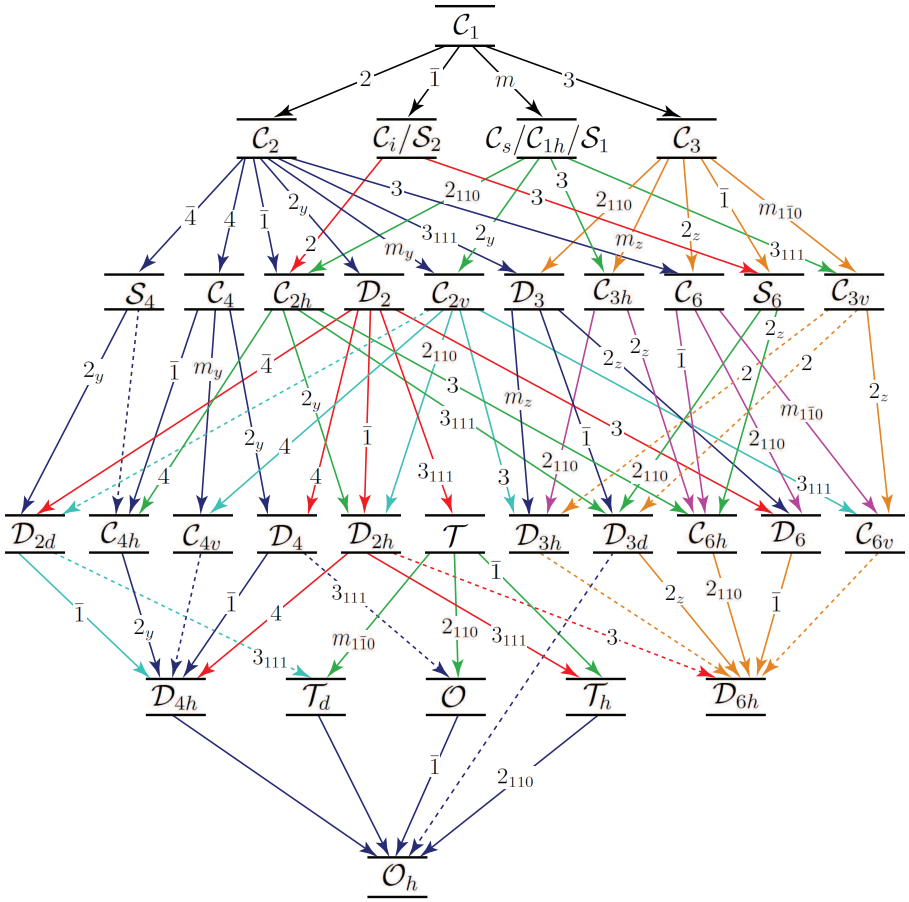

Figure A.2. All crystallographic point groups are shown along with their subgroup/overgroup relationships.

we may tend to think of the matrix as the operation or group element while really it is merely one way of representing the operation in question. It is thus also important to note that representation matrices are not unique, in general. It is possible to describe a particular symmetry operation as a matrix of more or less any dimension. Representations do, however, have a minimum dimensionality; these representations are in their *irreducible* form. Additionally, we will define the *character* of a representation as the trace of the matrix, and label it χ, which will grant us some insights later.

A.2.1 Irreducible Representations

The distinction between reducible and irreducible representations is made as follows. [92]

Definition A.1. *If by one and the same equivalence transformation, all of the matrices in the representation of a group can be made to acquire the same block form, then the representation is said to be reducible; otherwise, it is irreducible. An irreducible representation cannot be expressed in terms of representations of lower dimensionality.*

For example, this is the two-dimensional irreducible representation of the C_{3v} group we have been discussing, which is often labeled Γ_2.

$$e = \begin{pmatrix} 1 & 0 \\ 0 & 1 \end{pmatrix} \qquad \delta = \begin{pmatrix} -\frac{1}{2} & \frac{\sqrt{3}}{2} \\ -\frac{\sqrt{3}}{2} & -\frac{1}{2} \end{pmatrix} \qquad \zeta = \begin{pmatrix} -\frac{1}{2} & -\frac{\sqrt{3}}{2} \\ \frac{\sqrt{3}}{2} & -\frac{1}{2} \end{pmatrix}$$

$$\alpha = \begin{pmatrix} -1 & 0 \\ 0 & 1 \end{pmatrix} \qquad \beta = \begin{pmatrix} \frac{1}{2} & -\frac{\sqrt{3}}{2} \\ -\frac{\sqrt{3}}{2} & -\frac{1}{2} \end{pmatrix} \qquad \gamma = \begin{pmatrix} \frac{1}{2} & \frac{\sqrt{3}}{2} \\ \frac{\sqrt{3}}{2} & -\frac{1}{2} \end{pmatrix}$$

We can combine it with the one-dimensional trivial representation Γ_1

$$e = \alpha = \beta = \gamma = \delta = \zeta = \begin{pmatrix} 1 \end{pmatrix}$$

to obtain a reducible representation $\Gamma_R = \Gamma_1 + \Gamma_2$:

$$e = \begin{pmatrix} 1 & 0 & 0 \\ 0 & 1 & 0 \\ 0 & 0 & 1 \end{pmatrix} \qquad \delta = \begin{pmatrix} 1 & 0 & 0 \\ 0 & -\frac{1}{2} & \frac{\sqrt{3}}{2} \\ 0 & -\frac{\sqrt{3}}{2} & -\frac{1}{2} \end{pmatrix} \qquad \zeta = \begin{pmatrix} 1 & 0 & 0 \\ 0 & -\frac{1}{2} & -\frac{\sqrt{3}}{2} \\ 0 & \frac{\sqrt{3}}{2} & -\frac{1}{2} \end{pmatrix}$$

$$\alpha = \begin{pmatrix} 1 & 0 & 0 \\ 0 & -1 & 0 \\ 0 & 0 & 1 \end{pmatrix} \qquad \beta = \begin{pmatrix} 1 & 0 & 0 \\ 0 & \frac{1}{2} & -\frac{\sqrt{3}}{2} \\ 0 & -\frac{\sqrt{3}}{2} & -\frac{1}{2} \end{pmatrix} \qquad \gamma = \begin{pmatrix} 1 & 0 & 0 \\ 0 & \frac{1}{2} & \frac{\sqrt{3}}{2} \\ 0 & \frac{\sqrt{3}}{2} & -\frac{1}{2} \end{pmatrix}$$

The number of irreducible representations a group has is always equal to the number of its conjugacy classes. Our group C_{3v} had 3 conjugacy classes (identity, reflections, and rotations), and it must therefore have 3 irreducible representations. W have already identified two of them above; the third one is called Γ_1' (the naming conventions are explained in Section A.4) and looks like

$$e = \delta = \zeta = \left(1\right), \qquad \alpha = \beta = \gamma = \left(-1\right)$$

Further, irreducible representations abide by a few very specific rules. The most important of these is often referred to as the Wonderful Orthogonality Theorem, which has many useful consequences.

Theorem A.2. *Wonderful Orthogonality Theorem*

$$\sum_R D^{(\Gamma_j)}_{\mu\nu}(R)\, D^{\left(\Gamma_{j'}\right)}_{\nu'\mu'}\left(R^{-1}\right) = \frac{h}{\ell_j}\delta_{\Gamma_j,\Gamma_{j'}}, \delta_{\mu\mu'}, \delta_{\nu\nu'} \tag{A.1}$$

is obeyed for all the inequivalent, irreducible representations of a group, where the summation is over all h group elements $A_1, A_2, ..., A_h$ and ℓ_j and $\ell_{j'}$ are, respectively, the dimensionalities of representation Γ_j and $\Gamma_{j'}$. If the representations are unitary, the orthonormality relation becomes

$$\sum_R D^{(\Gamma_j)}_{\mu\nu}(R)\left[D^{\left(\Gamma_{j'}\right)}_{\mu'\nu'}(R)\right]^* = \frac{h}{\ell_j}\delta_{\Gamma_j,\Gamma_{j'}}, \delta_{\mu\mu'}, \delta_{\nu\nu'} \tag{A.2}$$

Here, D is a representation matrix for representation Γ_j with matrix elements indexed by μ and ν, R are the group elements, the * symbol indicates complex conjugation, and δ is the Kronecker delta. Let's see what this actually implies for our favorite group C_{3v}. Consider the orthogonality relationship between its two irreducible representations Γ_1 and $\Gamma_{1'}$. Expression A.2 evaluates to

$$\sum_R D^{(\Gamma_j)}_{\mu\nu}(R)\, D^{\left(\Gamma_{j'}\right)*}_{\mu'\nu'}(R) = (1\cdot 1) + (1\cdot 1) + (1\cdot 1) - (1\cdot 1) - (1\cdot 1) - (1\cdot 1) = 0 \tag{A.3}$$

There is a similar and related theorem for just the characters of irreducible representations, which will be incredibly useful for constructing character tables, which are described in Section A.3.

Theorem A.3. *Wonderful Orthogonality Theorem for Character*

$$\sum_k N_k \chi^{(\Gamma_j)}(\mathcal{C}_k) \left[\chi^{(\Gamma_{j'})}(\mathcal{C}_k)\right]^* = h\delta_{\Gamma_j,\Gamma_{j'}} \tag{A.4}$$

Here, $\mathcal{C}_k$ is one of the k conjugacy classes of the group, and N_k is the number of elements in that class, and $\chi^{(\Gamma_j)}(\mathcal{C}_k)$ is the primitive character of the elements of class $\mathcal{C}$ in irreducible representation Γ_j. This means that the character of two non-equivalent irreducible representations are orthogonal, and this only holds for primitive characters. We will again test this on the crystal group C_{3v}

$$\sum_k N_k \chi^{(\Gamma_j)}(\mathcal{C}_k) \left[\chi^{(\Gamma_{j'})}(\mathcal{C}_k)\right]^* = (1)(1)(1) + (3)(1)(-1) + (2)(1)(1) = 0 \tag{A.5}$$

This result is incredibly important because it tells us whether a representation is reducible or not – only irreducible representations will obey the orthogonality condition. Additionally, this lets us know whether or not we have found all of the irreducible representations of a group, given the expression (which relates the order of the group and the dimensionality of its irreducible representations)

$$\sum_j \ell_j^2 = h \tag{A.6}$$

where the sum is over all irreducible representations, h is the number of elements in the group and ℓ is the dimensionality of the representation. Lastly, character allows us to check for uniqueness because in order for two irreducible representations to be equivalent, their characters must be the same.

A.2.2 Reducible Representations

If we know nothing more about a group G than its multiplication table, we can always, at the very least, construct the matrices of its regular representation. These matrices are obtained by rearranging the rows and columns of the Cayley table such that the identity element always appears along the main diagonal. For the triangle group, such a rearrangement is shown in Table A.3 and is obtained simply by switching the last two rows. Then in order to attain the matrix representation for each element of the group, we copy the rearranged multiplication table into a matrix and replace all instances of a given element of the group with 1's and all other entries with 0's. Unsurprisingly, the regular representation matrix for the identity element e is

	e	α	β	γ	δ	ζ
e	e	α	β	γ	δ	ζ
α	α	e	ζ	δ	γ	β
β	β	δ	e	ζ	α	γ
γ	γ	ζ	δ	e	β	α
ζ	ζ	γ	α	β	e	δ
δ	δ	β	γ	α	ζ	e

Table A.3. Rearranged Cayley table for equilateral triangle symmetry group C_{3v}.

$$e = \begin{pmatrix} 1 & 0 & 0 & 0 & 0 & 0 \\ 0 & 1 & 0 & 0 & 0 & 0 \\ 0 & 0 & 1 & 0 & 0 & 0 \\ 0 & 0 & 0 & 1 & 0 & 0 \\ 0 & 0 & 0 & 0 & 1 & 0 \\ 0 & 0 & 0 & 0 & 0 & 1 \end{pmatrix}.$$

Meanwhile, the matrices for the reflection operations are

$$\alpha = \begin{pmatrix} 0 & 1 & 0 & 0 & 0 & 0 \\ 1 & 0 & 0 & 0 & 0 & 0 \\ 0 & 0 & 0 & 0 & 1 & 0 \\ 0 & 0 & 0 & 0 & 0 & 1 \\ 0 & 0 & 1 & 0 & 0 & 0 \\ 0 & 0 & 0 & 1 & 0 & 0 \end{pmatrix}, \beta = \begin{pmatrix} 0 & 0 & 1 & 0 & 0 & 0 \\ 0 & 0 & 0 & 0 & 0 & 1 \\ 1 & 0 & 0 & 0 & 0 & 0 \\ 0 & 0 & 0 & 0 & 1 & 0 \\ 0 & 0 & 0 & 1 & 0 & 0 \\ 0 & 1 & 0 & 0 & 0 & 0 \end{pmatrix}, \gamma = \begin{pmatrix} 0 & 0 & 0 & 1 & 0 & 0 \\ 0 & 0 & 0 & 0 & 1 & 0 \\ 0 & 0 & 0 & 0 & 0 & 1 \\ 1 & 0 & 0 & 0 & 0 & 0 \\ 0 & 1 & 0 & 0 & 0 & 0 \\ 0 & 0 & 1 & 0 & 0 & 0 \end{pmatrix},$$

and the rotation matrices look like

$$\zeta = \begin{pmatrix} 0 & 0 & 0 & 0 & 0 & 1 \\ 0 & 0 & 1 & 0 & 0 & 0 \\ 0 & 0 & 0 & 1 & 0 & 0 \\ 0 & 1 & 0 & 0 & 0 & 0 \\ 1 & 0 & 0 & 0 & 0 & 0 \\ 0 & 0 & 0 & 0 & 1 & 0 \end{pmatrix}, \delta = \begin{pmatrix} 0 & 0 & 0 & 0 & 1 & 0 \\ 0 & 0 & 0 & 1 & 0 & 0 \\ 0 & 1 & 0 & 0 & 0 & 0 \\ 0 & 0 & 1 & 0 & 0 & 0 \\ 0 & 0 & 0 & 0 & 0 & 1 \\ 1 & 0 & 0 & 0 & 0 & 0 \end{pmatrix}.$$

The identity, e, is the only regular representation matrix element that has a non-zero trace. In fact, its trace will always be equal to the order of the group. The following useful property of the regular representation technically allows us to find all of the irreducible representations of the group.

Theorem A.4. *The regular representation contains each irreducible representation a number of times equal to the dimensionality of the representation.*

However, to obtain the irreducible representations from the regular representation, we require a similarity transformation that brings these regular representations matrices into block diagonal form, which is generally an intractable problem. What we can use to our advantage though is the following.

Theorem A.5. *The reduction of any reducible representation into its reducible constituents is unique.*

This means that if for some class in some reducible representation, the non-primitive character is $\chi(\mathcal{C}_k)$, it can be written as a linear combination of the primitive characters of the irreducible representations of the group $\chi^(\Gamma_j)(\mathcal{C}_k)$ as follows

$$\chi\left(\mathcal{C}_k\right) = \sum_{\Gamma_i} a_i \chi^{(\Gamma_i)}\left(\mathcal{C}_k\right) \tag{A.7}$$

Here, a_i are unique, non-negative integers that correspond to the number of times the irreducible representation Γ_i is contained within the reducible representation we started with and are given by

$$a_i = \frac{1}{h} \sum_k N_k \left[\chi^{(\Gamma_i)}\left(\mathcal{C}_k\right)\right]^* \chi\left(\mathcal{C}_k\right). \tag{A.8}$$

A.3 Character Tables

The character table is a two-dimensional table in which the rows correspond to the irreducible representations of a group and the columns correspond to its conjugacy classes. The entries of the character table contain the character (trace of the irreducible representation matrices) of each class of group elements for every irreducible representation and are generally complex numbers. Character tables can be extremely useful in crystallography, chemistry, and spectroscopy for classifying phenomena according to their symmetry or, for example, determining if a transition between two states is forbidden due to symmetry. Because character tables for the crystal groups are well documented in books and tables, it is usually sufficient to simply look them up. However, one might want to construct the character table for an arbitrary crystal structure from scratch, in which case the following guidelines and procedure would be quite helpful. Most of the rules we need have already been introduced in the previous sections. The general procedure for generating arbitrary character tables is outlined in Section A.5, but we will begin by constructing a character table for the group C_{3v}. The empty table is shown in Table A.4. The rows label the irreducible representations with their special names, and the columns label the conjugacy classes. There is a special way to name conjugacy classes also, which is discussed in Section A.4. The number preceding the $\mathcal{C}$ corresponds to the number of elements in the class, so we can already infer from our earlier exercise that $\mathcal{C}_1$ is the identity class, $\mathcal{C}_2$ is the

mirror plane class, and $\mathcal{C}_3$ is the rotation class.

	$\mathcal{C}_1$	$3\mathcal{C}_2$	$2\mathcal{C}_3$
Γ_1			
$\Gamma_{1'}$			
Γ_2			

Table A.4. Empty character table for the equilateral triangle symmetry group C_{3v}.

The first step always is to fill the first row with 1's for the identity representation, as shown in Table A.5.

	$\mathcal{C}_1$	$3\mathcal{C}_2$	$2\mathcal{C}_3$
Γ_1	1	1	1
$\Gamma_{1'}$			
Γ_2			

Table A.5. The first row is always filled with 1's for the identity representation.

The numbers in the first column will be equal to the dimensionalities of the representations. The sum of their squares must be equal to the order of the group. In this case (and most others), there is only one way to satisfy that condition: $1^2+?^2+?^2 = 6 \Rightarrow 1^2 + 1^2 + 2^2 = 6$, as shown in Table A.6.

	$\mathcal{C}_1$	$3\mathcal{C}_2$	$2\mathcal{C}_3$
Γ_1	1	1	1
$\Gamma_{1'}$	1		
Γ_2	2		

Table A.6. The first column contains the dimensionalities of the representations.

Dimension 1 characters can only take on values of ± 1 (this is the trace of a one-dimensional matrix), and the rows of the character table must be orthogonal to each other, so let's look at rows Γ_1 and $\Gamma_{1'}$: $1(1 \cdot 1) + 3(1 \cdot ?) + 2(1 \cdot ?) = 0 \Rightarrow 1(1 \cdot 1) + 3(1 \cdot -1) + 2(1 \cdot 1) = 0$, as shown in Table A.7. As a side note, because we know that the class $\mathcal{C}_2$ contains mirror planes, which are an inverting operation, the trace of its matrices has to be negative.

	$\mathcal{C}_1$	$3\mathcal{C}_2$	$2\mathcal{C}_3$
Γ_1	1	1	1
$\Gamma_{1'}$	1	-1	1
Γ_2	2		

Table A.7. The orthogonality condition must be satisfied.

Lastly, the sum of the squares of the characters in any column must be equal to the order of the centralizer group for that class, so $1^+1^2+?^2 = 3$ and $1^2 + (-1)^2+?^2 = 2$, resulting in Table A.8. Not all character tables are this simple to complete, but all

	$\mathcal{C}_1$	$3\mathcal{C}_2$	$2\mathcal{C}_3$
Γ_1	1	1	1
$\Gamma_{1'}$	1	-1	1
Γ_2	2	0	-1

Table A.8. The centralizer condition must be satisfied.

character tables of crystallographic point groups are attainable using these theorems and constraints.

A.4 Naming Conventions

There is a fairly consistent collection of naming conventions that is used worldwide when discussing crystal group symmetry. In this section, we will discuss the notation standards for labeling symmetry operations, conjugacy classes, and irreducible representations.

A.4.1 Symmetry Operations and Conjugacy Classes

The symmetry operations of crystal groups are most commonly labeled according to either the Schoeflies system, often used by physicists, or the Hermann-Mauguin system, which is used by the crystallographers. We will briefly summarize both of them in Table A.9 though the Schoenflies notation will be used exclusively henceforth. An n-fold rotation is a rotation by $2\pi/n$ radians and can also be thought of as the structure having n equivalent orientations. The axis of highest symmetry is called the principal axis. Rotations about axes other than the principal axis are labeled C_n'; more primes are added to signify non-equivalent sets of non-principal axes, e.g. C_n''.The difference between the different types of mirror plane might not be readily apparent. The horizontal reflection plane, σ_h, is always normal to the principal rotation axis.

	Schoeflies	Hermann-Mauguin
n-fold rotation	C_n	n
n-fold rotoinversion	iC_n or S_n	$\bar{n}$
mirror plane	σ	m
horizontal reflection plane	σ_h	n/m
vertical reflection plane	σ_v	nm
non-equivalent vertical reflection planes	$\sigma_{v'}$	nmm

Table A.9. The Schoeflies and Hermann-Mauguin naming conventions for symmetry group elements.

Vertical reflection planes, σ_v, contain the principal rotation axis, and non-equivalent reflection planes are labeled σ_v'. Dihedral planes are sometimes labeled σ_d. The naming convention for conjugacy classes is basically the same because they represent sets of similar operations. Each class's name is generated by preceding the name of the symmetry operation it represents by a number that indicates the number of operations in the class, e.g. the mirror plane class of C_{3v} is called $3\sigma_v$. The identity and inversion operations always have their own classes and are labeled E and i, respectively.

A.4.2 Irreducible Representations

The notation used for the labeling of irreducible representations was introduced by Mulliken and is summarized in Tables A.10 and A.11.

Labels	
A	one-dimensional representation symmetric with respect to rotation by $2\pi/n$ about the principal axis
B	one-dimensional representation antisymmetric with respect to rotation by $2\pi/n$ about the principal axis
E	two-dimensional representation
T	three-dimensional representation

Table A.10. Labels for irreducible representations.

A.5 CASM Implementation

Cluster Assisted Statistical Mechanics (CASM) is a living, evolving software package developed by the Van der Ven group. CASM's ever-increasing suite of features includes the capability to generate crystal structures by enumerating symmetrically unique configurations of any number of species on a given lattice (for studying disorder

Subscripts	
g	odd parity in groups containing inversion
u	even parity in groups containing inversion
1	symmetry with respect to C_2 axis normal to the principal axis or vertical mirror plane
2	antisymmetry with respect to C_2 axis normal to the principal axis or vertical mirror plane
$'$	symmetry with respect to horizontal mirror plane
$''$	antisymmetry with respect to horizontal mirror plane

Table A.11. Subscripts to irreducible representation labels.

and phase transitions), a number of statistical mechanics tools for carrying out grand canonical Monte Carlo (to calculate thermodynamic properties) and kinetic Monte Carlo (for transport properties) simulations, and more. CASM's symmetry packages are able to calculate the point groups and factor groups of any structure and to determine and properly label their character tables. The algorithms to accomplish this are documented in Figures A.3–A.5.

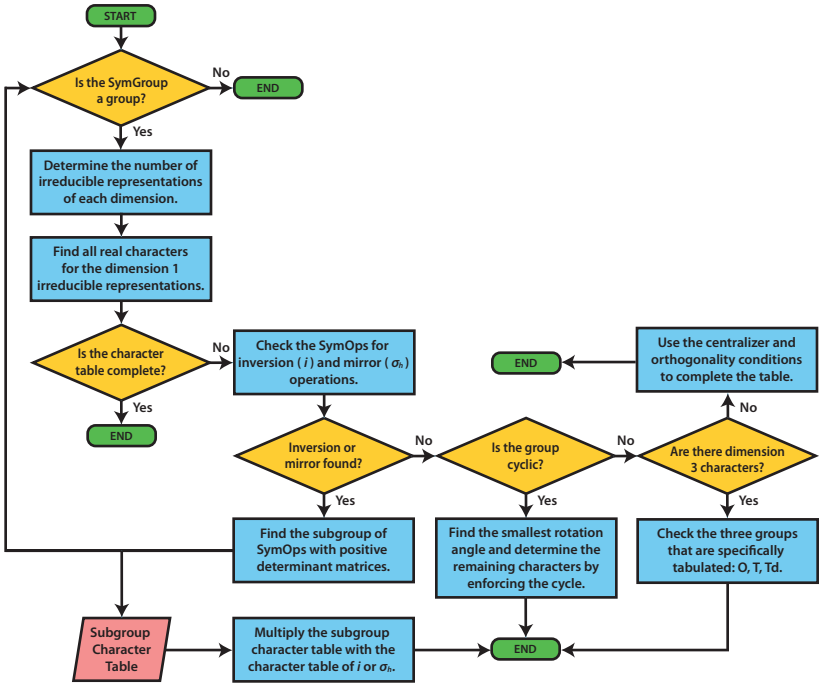

Figure A.3. Flow chart for the algorithm to generate the character table of a crystal symmetry group within CASM. SymGroup is a symmetry group object, which contains symmetry operation objects called SymOps.

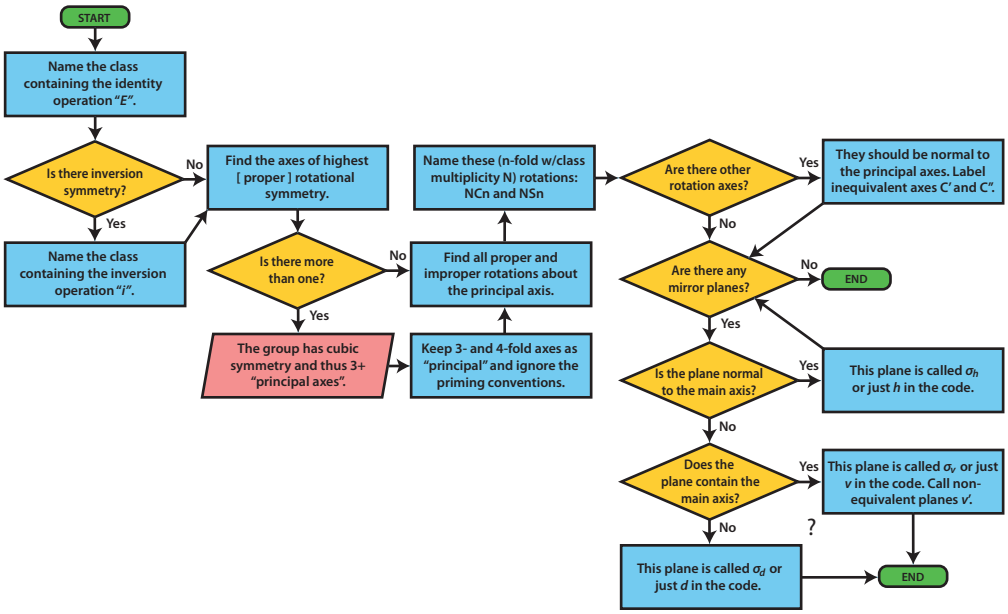

Figure A.4. Flow chart for the algorithm to assign names for the conjugacy classes of a symmetry group, provided the SymGroup object has been correctly initialized and populated with symmetry operations.

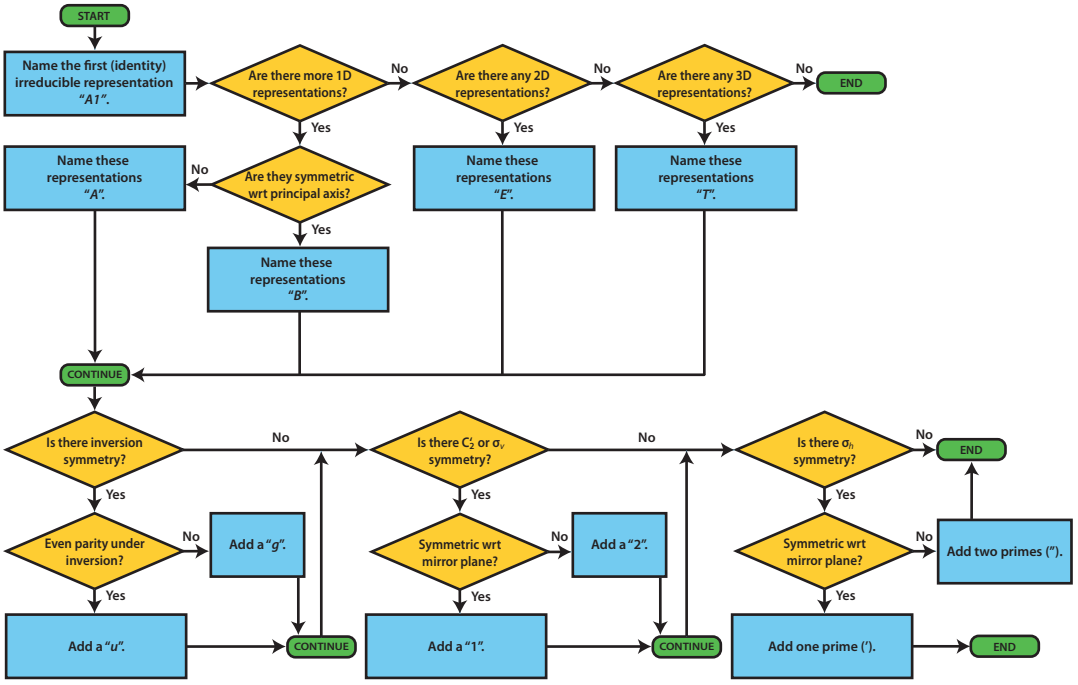

Figure A.5. Flow chart for the algorithm to assign names to irreducible representations of a symmetry group, provided the character table has already been generated correctly.

BIBLIOGRAPHY

BIBLIOGRAPHY

[1] D.R. Hartree, "The wave mechanics of an atom with a non-coulomb central field. part i. theory and methods," *Mathematical Proceedings of the Cambridge Philosophical Society*, **24**, pp. 89–110, (1928).

[2] N. Metropolis and S. Ulam, "The Monte Carlo method," *Journal of the American Statistical Association*, **44**, pp. 335–341, (1949).

[3] A.A. Belak, Y.Z. Wang, and A. Van der Ven, "Kinetics of anatase electrodes: The role of ordering, anisotropy, and shape memory effects," *Chem. Mater.*, **24**, pp. 2894–2898, (2012).

[4] Y.-W. Kim, "Ordered intermetallic alloys, part iii: Gamma titanium aluminides," *J. Metals*, **46**, p. 30, (1994).

[5] F. Appel, P.A. Beaven, and R. Wagner, "Deformation processes related to interfacial boundaries in two-phase γ-titanium aluminides," *Acta Metallurgica et Materialia*, **41**, pp. 1721–1732, (1993).

[6] J.L. Murray, *Phase Diagrams of Binary Titanium Alloys.* ASM International, (1987).

[7] J.C. Schuster and M. Palm, "Reassessment of the binary aluminum-titanium phase diagram," *J. Phase Equilib.*, **27**, pp. 255–277, (2006).

[8] H.B. Callen, *Thermodynamics and an Introduction to Thermostatistics.* New York: John Wiley and Sons, 2nd ed., (1985).

[9] D.A. McQuarrie, *Statistical Thermodynamics.* University Science Books, (1973).

[10] M. Born and J.R. Oppenheimer, "Zur Quantentheorie der Molekeln (On the quantum theory of molecules)," *Ann. Physik*, **389**, p. 457, (1927).

[11] R.A. Evarestov, *Quantum Chemistry of Solids: The LCAO First Principles Treatment of Crystals.* Solid State Sciences, Berlin: Springer-Verlag, (2007).

[12] P. Hohenberg and W. Kohn, "Inhomogeneous electron gas," *Phys. Rev.*, **136**, p. B864, (1964).

[13] W. Kohn and L.J. Sham, "Self-consistent equations including exchange and correlation effects," *Phys. Rev.*, **140**, p. A1133, (1965).

[14] K. Capelle, "A bird's-eye view of density-functional theory," *arXiv:cond-mat/0211443v5 [cond-mat.mtrl-sci]*, (2006).

[15] J.P. Perdew and A. Zunger, "Self-interaction correction to density-functional approximations for many-electron systems," *Phys. Rev. B*, **23**, p. 5048, (1981).

[16] J.P. Perdew, K. Burke, and M. Ernzerhof, "Generalized gradient approximation made simple," *Phys. Rev. Lett.*, **77**, p. 3865, (1996).

[17] J.P. Perdew, K. Burke, and M. Ernzerhof, "Erratum: Generalized gradient approximation made simple," *Phys. Rev. Lett.*, **78**, p. 1396, (1997).

[18] G. Kresse and J. Furthmuller, "Efficiency of ab-initio total energy calculations for metals and semiconductors using a plane-wave basis set," *Computational Materials Science*, **6**, pp. 15–50, (1996).

[19] G. Kresse and J. Furthmuller, "Efficient iterative schemes for ab initio total-energy calculations using a plane-wave basis set," *Phys. Rev. B*, **54**, pp. 11169–11186, (1996).

[20] G. Kresse and D. Joubert, "From ultrasoft pseudopotentials to the projector augmented-wave method," *Phys. Rev. B*, **59**, pp. 1758–1775, (1999).

[21] P.E. Blochl, "Projector augmented-wave method," *Phys. Rev. B*, **50**, p. 17953, (1994).

[22] J.M. Sanchez, F. Duscatelle, and D. Gratias, "Generalized cluster description of multicomponent systems," *Physica A*, **128**, p. 334, (1984).

[23] A. van de Walle and G. Ceder, "Automating first-principles phase diagram calculations," *J. Phase Equilib.*, **23**, pp. 391–394, (2002).

[24] B. Puchala and A. Van der Ven, "Thermodynamics of the Zr-O system from first-principles calculations," *Phys. Rev. B*, **88**, p. 094108, (2013).

[25] N. Metropolis, A.W. Rosenbluth, M.N. Rosenbluth, A.H. Teller, and E. Teller, "Equation of state calculations by fast computing machines," *J. Chem. Phys.*, **21**, pp. 1087–1092, (1953).

[26] R. Gomer, "Diffusion of adsorbates on metal surfaces," *Rep. Prog. Phys.*, **53**, p. 917, (1990).

[27] J. Bhattacharya and A. Van der Ven, "Phase stability and nondilute Li diffusion in spinel $Li_{1+x}Ti_2O_4$," *Phys. Rev. B*, **81**, p. 104304, (2010).

[28] A. Van der Ven, G. Ceder, M. Asta, and P.D. Tapesch, "First-principles theory of ionic diffusion with nondilute carriers," *Phys. Rev. B*, **64**, p. 184307, (2001).

[29] L. Kavan, M. Gratzel, S.E. Gilbert, C. Klemenz, and H.J. Scheel, "Electrochemical and photoelectrochemical investigation of single-crystal anatase," *J. Am. Chem. Soc.*, **118**, p. 6716, (1996).

[30] M. Gratzel, "Solar energy conversion by dye-sensitized photovoltaic cells," *Inorg. Chem.*, **44**, p. 6841, (2005).

[31] T. Ohzuku and T. Hirai, "An electrochromic display based on titanium dioxide," *Elechtrochim. Acta.*, **27**, p. 1263, (1982).

[32] F. Bonino, L. Busani, M. Lazzari, M. Manstretta, B. Rivolta, and B. Scrosati, "Anatase as a cathode material in lithium-organic electrolyte rechargeable batteries," *J. Power Sources*, **6**, p. 261, (1981).

[33] T. Ohzuku, Z. Takehara, and S. Yoshizawa, "Non-aquaeous lithium-titanium dioxide cell," *Electrochim. Acta*, **24**, p. 219, (1979).

[34] T. Ohzuku, T. Kodama, and T. Hirai, "Electrochemistry of anatase titanium dioxide in lithium nonaqueaous cells," *J. Power Sources*, **14**, p. 153, (1985).

[35] W.J. Macklin and R.J. Neat, "Performance of titanium dioxide-based cathodes in a lithium polymer electrolyte cell," *Solid State Ionics*, **53**, p. 694, (1992).

[36] S.Y. Huang, L. Kavan, I. Exnar, and M. Gratzel, "Rocking chair lithium battery based on nanocrystalline TiO_2 (anatase)," *J. Electrochem. Soc.*, **142**, p. L142, (1995).

[37] M.S. Whittingham and M.B. Dines, "n-Butyllithium – an effective, general cathode screening agent," *J. Electrochem. Soc.*, **124**, p. 1387, (1977).

[38] B. Zachau-Christiansen, K. West, T. Jacobsen, and S. Atlung, "Lithium insertion in different TiO_2 modifications," *Solid State Ionics*, **28-30**, p. 1176, (1988).

[39] W.J.H. Borghols, D. Lutzenkirchen-Hecht, U. Haake, E.R.H. van Eck, F.M. Mulder, and M. Wagemaker, "The electronic structure and ionic diffusion of nanoscale $LiTiO_2$ anatase," *Phys. Chem. Chem. Phys.*, **11**, p. 5742, (2009).

[40] M. Wagemaker, G. Kearley, A.A. van Well, H. Mutka, and F.M. Mulder, "Multiple Li positions inside oxygen octahedra in lithiated TiO_2 anatase," *J. Am. Chem. Soc.*, **125**, p. 840, (2003).

[41] A.S. Dalton, A.A. Belak, and A. Van der Ven, "Thermodynamics of lithium in TiO_2(B) from," *Chem. Mater.*, **24**, pp. 1568–1574, (2012).

[42] A. Van der Ven, J.C. Thomas, Q. Xu, and B. Swoboda, "Nondilute diffusion from first principles: Li diffusion in Li_xTiS_2," *Phys. Rev. B*, **78**, p. 104306, (2008).

[43] B.J. Morgan and G.W. Watson, "Role of lithium ordering in the Li_xTiO_2 anatase $\rightarrow$ titanate phase transition," *J. Phys. Chem. Lett.*, **2**, p. 1657, (2011).

[44] M. Wagemaker, W.J.H. Borghols, and F.M. Mulder, "Large impact of particle size on insertion reactions. a case for anatase Li_xTiO_2," *J. Am. Chem. Soc.*, **129**, p. 4323, (2007).

[45] D.W. Murphy, R.J. Cava, S.M. Zahurak, and A. Santoro, "Ternary Li_xTiO_2 phases from insertion reactions," *Solid State Ionics*, **9-10**, p. 413, (1983).

[46] R.J. Cava, D.W. Murphy, S. Zahurak, A. Santoro, and R.S. Roth, "The crystal-structures of the Lithium-inserted metal-oxides $Li_{0.5}TiO_2$ anatase, $LiTi_2O_4$ spinel, and $Li_2Ti_2O_4$," *J. Solid State Chem.*, **53**, p. 64, (1984).

[47] J. Bhattacharya and A. Van der Ven, "First-principles study of competing mechanisms of nondilute Li diffusion in spinel Li_xTiS_2," *Phys. Rev. B*, **83**, p. 144302, (2011).

[48] A. Van der Ven, J. Bhattacharya, and A.A. Belak, "Understanding Li diffusion in Li-intercalation compounds," *Acc. Chem. Res.*, **46**, p. 1216, (2013).

[49] B.J. Morgan and G.W. Watson, "GGA+U description of lithium intercalation into anatase TiO_2," *Phys. Rev. B*, **82**, p. 144119, (2010).

[50] G. Sudant, E. Baudrin, D. Larcher, and J.-M. Tarascon, "Electrochemical lithium reactivity with nanotextured anatase-type TiO_2," *J. Mater. Chem.*, **15**, p. 1263, (2005).

[51] J.-Y. Shin, D. Samuelis, and J. Maier, "Sustained lithium-storage performance of hierarchical, nanoporous anatase TiO_2 at high rates: Emphasis on interfacial storage phenomena," *Adv. Funct. Mater.*, **21**, p. 3464, (2013).

[52] D. Bresser, E. Paillard, E. Binetti, S. Krueger, M. Striccoli, M. Winter, and S. Passerini, "Percolating networks of TiO_2 nanorods and carbon for high power lithium insertion electrodes," *J. Power Sources*, **206**, p. 301, (2012).

[53] A. Van der Ven, K. Garikipati, S. Kim, and M. Wagemaker, "The role of coherency strains on phase stability in Li_xFePO_4: Needle crystallites minimize coherency strain and overpotential," *J. Electrochem. Soc.*, **156**, p. A949, (2009).

[54] J.W. Christian, "Crystallographic theories, interface structures, and transformation mechanisms," *Metall. Mater. Trans. A*, **25**, p. 1821, (1994).

[55] C. Freysoldt, B. Grabowski, T. Hickel, J. Neugebauer, G. Kresse, A. Janotti, and C.G. Van de Walle, "First-principles calculations for point defects in solids," *Rev. Mod. Phys.*, **86**, p. 253, (2014).

[56] S.B. Zhang, S.H. Wei, A. Zunger, and H. Katayama-Yoshida, "Defect physics of the $CuInSe_2$ chalcopyrite semiconductor," *Phys. Rev. B*, **57**, pp. 9642–9656, (1998).

[57] A.F. Kohan, G. Ceder, D. Morgan, and C.G. Van de Walle, "First-principles study of native point defects in ZnO," *Phys. Rev. B*, **61**, p. 15019, (2000).

[58] S.B. Zhang, S.H. Wei, and A. Zunger, "Intrinsic n-type versus p-type doping asymmetry and the defect physics of ZnO," *Phys. Rev. B*, **63**, p. 075205, (2001).

[59] C.G. Van de Walle and J. Neugebauer, "First-principles calculations for defects and impurities: Applications to III-nitrides," *J. Appl. Phys.*, **95**, p. 3851, (2004).

[60] A. Janotti and C.G. Van de Walle, "Oxygen vacancies in ZnO," *Phys. Rev. B*, **87**, p. 122102, (2005).

[61] A. Janotti and C.G. Van de Walle, "Native point defects in ZnO," *Phys. Rev. B*, **76**, p. 165202, (2007).

[62] T.M. Pollock and S. Tin, "Nickel-based superalloys for advanced turbine engines: Chemistry, microstructure and properties," *J. Propul. Power*, **22**, pp. 361–374, (2006).

[63] T.M. Pollock, J. Dibbern, M. Tsunekane, J. Zhu, and A. Suzuki, "New Co-based $\gamma - \gamma$' high-temperature alloys," *JOM*, **62**, pp. 58–63, (2010).

[64] G.J. Snyder and E.S. Toberer, "Complex thermoelectric materials," *Nature Materials*, **7**, pp. 105–114, (2008).

[65] J. Androulakis, C.H. Lin, H.J. Kong, C. Uher, C.I. Wu, T. Hogan, B.A. Cook, T. Caillat, K.M. Paraskevopoulos, and M.G. Kanatzidis, "Spinodal decomposition and nucleation and growth as a means to bulk nanostructure thermoelectrics: Enhanced performance in $Pb_{1-x}Sn_xTe$-PbS," *J. Am. Chem. Soc.*, **129**, pp. 9780–9788, (2007).

[66] H. Chi, H. Kim, J.C. Thomas, X.L. Su, S. Stackhouse, M. Kaviany, A. Van der Ven, X.F. Tang, and C. Uher, "Configuring pnicogen rings in skutterudites for low phonon conductivity," *Phys. Rev. B*, **86**, p. 195209, (2012).

[67] H. Kim, M. Kaviany, J.C. Thomas, A. Van der Ven, C. Uher, and B.L. Huang, "Structural order-disorder transitions and phonon conductivity of partially filled skutterudites," *Phys. Rev. Lett.*, **105**, p. 265901, (2010).

[68] A. Emly, E. Kioupakis, and A. Van der Ven, "Phase stability and transport mechanisms in antiperovskite Li_3OCl and Li_3OBr superionic conductors," *Chem. Mater.*, **25**, pp. 4663–4670, (2013).

[69] A. Van der Ven, H.C. Yu, G. Ceder, and K. Thornton, "Vacancy mediated substitutional diffusion in binary crystalline solids," *Progress in Materials Science*, **55**, pp. 61–105, (2010).

[70] A.D. Smigelskas and E.O. Kirkendall, "Zinc diffusion in alpha-brass," *Transactions of the American Institute of Mining and Metallurgical Engineering*, **171**, pp. 130–142, (1947).

[71] Y.D. Yin, R.M. Rioux, C.K. Erdonmez, S. Hughes, G.A. Somorjai, and A.P. Alivisatos, "Formation of hollow nanocrystals through the nanoscale Kirkendall Effect," *Science*, **304**, pp. 711–714, (2004).

[72] A.G. Evans, D.R. Mumm, J.W. Hutchinson, G.H. Meier, and F.S. Pettit, "Mechanisms controlling the durability of thermal barrier coatings," *Progress in Materials Science*, **46**, pp. 505–553, (2001).

[73] T.M. Pollock, D.M. Lipkin, and K.J. Hemker, "Multifunctional coating interlayers for thermal-barrier systems," *MRS Bulletin*, **37**, pp. 923–931, (2012).

[74] M. Asta, C. Wolverton, H. de Fontaine, and H. Dreysse, "Effective cluster interactions from cluster-variation formalism i," *Phys. Rev. B*, **44**, pp. 4907–4913, (1991).

[75] J.M. Sanchez, "Cluster expansion and the configurational theory of alloys," *Phys. Rev. B*, **81**, p. 224202, (2010).

[76] G. Inden and G. Kostorz, *Phase Tranformations in Materials.* Wiley-VCH, (2001).

[77] G.L.W. Hart, V. Blum, M.J. Walorski, and A. Zunger, "Evolutionary approach for determining first-principles hamiltonians," *Nature Materials*, **4**, pp. 391–394, (2005).

[78] A. Van der Ven, "First-principles investigation of phase stability in Li_xCoO_2," *Phys. Rev. B*, **58**, pp. 2975–2987, (1998).

[79] U.R. Kattner, J.C. Lin, and Y.A. Chang, "Thermodynamic assessment and calculation of the Ti-Al system," *Metallurgical Transactions A – Physical Metallurgy and Materials Science*, **23**, pp. 2081–2090, (1992).

[80] I. Ohnuma, Y. Fujita, H. Mitsui, K. Ishikawa, R. Kainuma, and K. Ishida, "Phase equilibria in the Ti-Al binary system," *Acta Mater.*, **48**, pp. 3113–3123, (2000).

[81] R. Kainuma, M. Palm, and G. Inden, "Solid-phase equilibria in the Ti-rich part of the Ti-Al system," *Intermetallics*, **2**, pp. 321–332, (1994).

[82] J.Y. Huh, J.M. Howe, and W.C. Johnson, "Effect of coherency stresses on the $\alpha+\alpha_2$ phase equilibria in Ti-Al alloys," *Acta Metall. Mater.*, **41**, p. 2577, (1993).

[83] P.W. Voorhees and W.C. Johnson, "The thermodynamics of elastically stressed crystals," *Solid State Physics*, **59**, pp. 1–201, (2004).

[84] J.W. Cahn and F. Larche, "A simple model for coherent equilibrium," *Acta Metall.*, **32**, p. 1915, (1984).

[85] J.Y. Lim, C.J. McMahon, D.P. Pope, and J.C. Williams, "The effect of oxygen on the structure and mechanical behavior of aged Ti-8 wt. pct. Al," *Metall. Trans.*, **7A**, pp. 139–144, (1976).

[86] A. Van de Walle, "Methods for first-principles alloy thermodynamics," *JOM*, **65**, pp. 1523–1532, (2013).

[87] Y. Mishin and Chr. Herzig, "Diffusion in the Ti-Al system," *Acta Materialia*, **48**, pp. 589–623, (2000).

[88] R. Wurschum, E.A. Kummerle, K. Badua-Gergen, A. Seeger, Chr. Herzig, and H.E. Schaefer, "Thermal vacancy formation and positron-vacancy interaction in Ti_3Al at high temperatures," *J. Appl. Phys.*, **80**, p. 724, (1996).

[89] A. Van der Ven and G. Ceder, "First principles calculation of the interdiffusion coefficient in binary alloys," *Phys. Rev. Lett.*, **94**, p. 045901, (2005).

[90] Q. Xu and A. Van der Ven, "Atomic transport in ordered compounds mediated by local disorder: diffusion in B2-Ni_xAl_{1-x}," *Phys. Rev. B*, **81**, p. 064303, (2010).

[91] A. Van der Ven and G. Ceder, "Vacancies in binary alloys treated with the cluster expansion," *Phys. Rev. B*, **71**, p. 054102, (2005).

[92] M.S. Dresselhaus, G. Dresselhaus, and A. Jorio, *Group Theory: Application to the Physics of Condensed Matter*. Berlin: Springer-Verlag, (2008).